PERGAMON

International Journal of Rock Mechanics & Mining Sciences 38 (2001) 995–1027

International Journal of
Rock Mechanics
and Mining Sciences

www.elsevier.com/locate/ijrmms

Bayesian estimation of rock mass boundary conditions with applications to the AECL underground research laboratory

F. Tonon*,[1], B. Amadei, E. Pan, D.M. Frangopol

Department of Civil Engineering, University of Colorado, Boulder, CO 80309-0428, USA

Accepted 22 June 2001

Abstract

In this paper, the estimation of boundary conditions for rock mass models is addressed by means of Bayesian identification procedures. Basic information can consist of stress, strain, or displacement measurements. Previous information is accounted for, so that boundary conditions can be updated at the various stages of a project, as soon as new information becomes available. For linearly elastic rock masses, the boundary conditions are computed in a one-step solution. For rock masses with non-linear behavior, an iterative procedure must be followed. Potential advantages and shortcomings are also discussed, together with comparisons with other methods available in the literature. The proposed procedure is applied to two(2)- and three-dimensional (3-D) non-linear models of the Underground Research Laboratory (URL) of the Atomic Energy of Canada Limited (AECL), Canada. The procedure displayed fast convergence despite the complex geometry of the site, and the high degree of non-linearity of the models. The 3-D model was able to completely reproduce the complex measured stress pattern, and the 90° rotation of the principal in situ stresses with depth. In order to reliably estimate the boundary conditions reproducing the current in situ state of stress, response measurements of the rock mass to current disturbances are necessary as input data.

1. Introduction

The US National Committee on Rock Mechanics offered the following definition of Rock Mechanics [1]: ''Rock Mechanics is the theoretical and applied science of the mechanical behavior of rock and rock masses; it is that branch of mechanics concerned with the response of rock and rock masses to the force fields of their physical environment''.

Thus, any rock mechanics study starts with the determination of the force fields in which the rock mass under study is embedded. Body forces and boundary conditions determine these force fields. The latter fields may be very complex, due to local variations in rock mass structure (petrography, discontinuities, heterogeneities, folds, faults, dikes, fabric, etc.), or to major structural features, such as faults at the regional scale. Faults may define stress domains at a large scale and cause rotations of principal stress directions.

In the majority of the cases, the boundary conditions are assumed (no lateral strain, uniform ''far field'' state of stress etc.). At best, they are derived by averaging the results of some (local) stress measurements over the volume of rock of interest, which, in the case of civil and mining projects, can be of the order of 10^3–$10^9\,m^3$. In fact, conventional stress measurement techniques (overcoring, borehole slotting, etc.) aim to determine local stress tensors, and involve only a few cubic meters of rock; thus, due to the aforementioned local variations in the force fields, this averaging exercise may be highly misleading [2].

Hence, the central question is how to assign boundary conditions to a (numerical) model of a rock mass, which, in the following, will be called $\mathfrak{M}$, for brevity. $\mathfrak{M}$ is the tool that allows one to forecast the rock mass response to any disturbance (e.g. excavation, slope, foundation etc.), and it is assumed to represent the main mechanisms governing the rock mass behavior [3,4].

In this paper, it is proposed to adopt a Bayesian approach in order to determine the boundary conditions

*Corresponding author. 1325, 15th Street NW, Apt.1017, Washington, DC 20005, USA. Tel.: +1-202-667-5968; fax: +1-202-667-3584.
E-mail address: fulvio@rcn.com (F. Tonon).
[1] Vicolo S. Antonino A, 3; I-31100 Treviso, Italy.

1365-1609/01/$ - see front matter
PII: S1365-1609(01)00036-3

for $\mathfrak{M}$. The rationale behind this choice is as follows: if information exists on the rock mass response to disturbances (e.g. measurements of strains, stresses, displacements), then this information may be used to identify the boundary conditions for $\mathfrak{M}$ that allow the response of $\mathfrak{M}$ to best fit the observed data. In civil engineering projects, actual observations are affected by the following factors: uncertainty, the need for updating information at different stages of a project (e.g. feasibility, preliminary, final, or construction stages), and the need for combining different sources of information (e.g. geological description and field measurements) as well as different types of information (e.g. intuitive or subjective assumption and experimental observations).

Within Probability Theory, the proper vehicle for this combination is Bayes' Theorem [5]. In this context, the probability of an event B_j before new information A becomes available is called "prior", or a priori, probability, whereas the probability of B_j after new information A becomes available is called "posterior", or a posteriori, probability. In words, Bayes' Theorem states that [6]:

$$\begin{bmatrix}\text{Posterior probability}\\ \text{of } B_j \text{ given the new}\\ \text{information, } A\end{bmatrix} = \begin{bmatrix}\text{Likelihood of the}\\ \text{new information,}\\ A, \text{ given } B_j\end{bmatrix} \times \begin{bmatrix}\text{Prior probability}\\ \text{of } B_j\end{bmatrix} \times \begin{bmatrix}\text{Normalizing}\\ \text{factor}\end{bmatrix}.$$

Let $P[.]$ denote the probability of an event, and $P[B|A]$ the conditional probability of B given that A has occurred. In symbols, Bayes' Theorem states that:

$$P[B_j|A] = \frac{P[A|B_j]P[B_j]}{\sum_{k=1}^{n} P[A|B_k]P[B_k]}.$$

For example, Ref. [6] gives a review of Bayes' Theorem applications in engineering geology.

At the outset of the present paper, a procedure is proposed for determining boundary conditions in linearly elastic rock masses. Subsequently, the procedure is extended to include the effect of material non-linearities. Advantages and limitations of the procedures proposed are discussed in detail. Comparisons are presented with other methods available in the literature.

Subsequently, the procedure for boundary condition estimation is applied to the site of the Underground Research Laboratory (URL), Canada. This application is deemed appropriate because of the wealth of available stress measurements, and the presence of interesting features such as different stress domains and reverse faults. Both 2-D and 3-D non-linear models of the URL site are considered, and the results contrasted.

In this paper, italic capital letters will be used for random variables, and lower case letters for the values they can assume. As detailed in the Appendix, the symbol $E[.]$ denotes the expected value of a quantity.

2. Remarks on some methods proposed in the literature

The importance of the concept of stress in the following considerations calls for some clarifications. Cornet [7] distinguishes between two stress concepts:

(a) Local stress tensor, defined at any point in a rock mass by the components of the mean surface traction supported by the smallest cube which completely surrounds the Representative Elementary Volume (REV). A REV, if it exists, is defined by the following properties: (1) In the REV a continuous material equivalent to the real material filling this volume is defined by its density and its porosity. These quantities are continuous functions. (2) The REV is small as compared to the gradients of the various variables involved by the mechanics of this equivalent continuum, so that these variables may be assumed to be constant within the REV. (3) There is no significant body force nor any resultant moment acting on the REV, so that the surface tractions acting on it can be used to define the components of a symmetrical stress tensor defined at the center of the REV. Condition (3) imposes an upper limit to the REV size: for too large a REV, body forces and resultant moment cannot be neglected. Because of this condition, for some rock masses a local stress tensor cannot be defined. The mechanics of such formations cannot be approached efficiently through continuum theory, and stress measurements should not be attempted.
(b) Regional stress field, defined as the set of six functions of the space coordinates describing the variation of the local stress tensor over the domain of interest.

Note that, throughout this paper, "stress" refers to the local stress concept.

The "Integrated Stress Determination Approach", ISDA, [8] relies on a non-linear, least-squares approach [9] to determine the regional stress field based on local stress measurements. However, strong assumptions are involved in the ISDA, namely: (i) lateral (i.e. horizontal) variations of stress can be neglected; (ii) the vertical direction is a principal direction throughout the volume of interest; (iii) the volume in which the regional stress field is computed is small enough for neglecting rotations of principal stress directions; (iv) the regional stress field is assumed to be continuous up to the ground surface. An advantage of the ISDA is that no

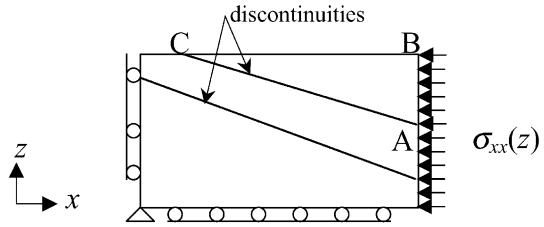

Fig. 1. Schematic of a rock mass model $\mathfrak{M}$ with applied stress boundary conditions.

assumption is necessary about the rock mass behavior (e.g. linearly elastic, elasto-plastic, etc.).

The regional stress field determined by the ISDA can be used as a boundary condition for $\mathfrak{M}$ only when stress boundary conditions are applicable, and the aforementioned assumptions (i) to (iv) hold for $\mathfrak{M}$. For example, stress boundary conditions are not applicable when discontinuities dissect the rock mass into kinematically unconstrained blocks, and boundary conditions must be applied to these blocks. To illustrate, consider the schematic 2-D model $\mathfrak{M}$ shown in Fig. 1, where $\sigma_{xx}(z)$ is determined by means of the ISDA. If the shear resistance along joint AC is overcome, then slippage occurs, block ABC accelerates and no static solution is possible. Consequently, if $\mathfrak{M}$ is to represent the current situation of a portion of the Earth crust at rest, the stress boundary condition shown in Fig. 1 is not applicable.

The in situ stress determination using the Under-Excavation Technique (UET) developed by Wiles and Kaiser [10,11] is halfway between local stress measurements and the regional stress field concept. In this method, the pre-existing in situ state of stress is determined by means of an identification procedure. The input data is the rock mass response to an advancing excavation; thus the UET can involve several hundred or more cubic meters of rock. In the identification procedure, a far field state of stress is determined that provides the "best fit" to the measured displacement and strain changes occurring as an excavation is extended. The analysis procedure is conducted in two distinct phases:

(a) A Boundary Element program is used to determine the functional relationship between the far field state of stress and the local stress and displacement changes at the measurement devices. The rock mass is assumed to be homogeneous and linearly elastic.
(b) The far field stress is determined by minimizing the sum of the squares of the differences between predicted and measured strain/displacement changes by means of the least squares method [12].

The UET actually determines the (stress) boundary conditions for the following model: a linearly elastic, homogeneous rock mass of infinite extent surrounding the monitored excavation. Whenever the rock mass model of interest, $\mathfrak{M}$, differs from the UET's, the boundary conditions for $\mathfrak{M}$ are left unspecified.

The UET allows a fundamental aspect of the problem in hand to be pinpointed, namely the dependence of the boundary conditions on $\mathfrak{M}$. Consequently, it is necessary to use $\mathfrak{M}$ in any identification technique of the boundary conditions. This concept is well known in identification theory, and was clearly stated by Gioda and Maier [13]: "in practical situations it is generally more convenient to perform, for identification purposes, particular applications of the general computer program to be employed, anyway, for the subsequent analysis, rather than to make recourse to an *ad hoc* formulation of the model."

In the preceding, the word "identification" was used, rather than "back analysis. " In fact, following Sakurai [14], and with reference to Fig. 2, the following three different procedures can be distinguished:

(1) In a forward analysis, once a mechanical model is assumed, and the values of the mechanical parameters are determined, then displacements, stresses and strains can be calculated.
(2) In an identification procedure, displacements, stresses and strains are measured, a mechanical model is assumed, and then the values of the mechanical parameters are calculated.
(3) In a back analysis, displacements, stresses and strains are measured, and then the model as well as the values of the mechanical parameters are determined.

The identification of structure, mechanical parameters, or inclusions of a rock mass has received much attention in the engineering literature (e.g. Refs. [3,13,15,16]), and, obviously, in the geophysics literature (e.g. Refs. [12,17,18]). As exemplified above, the determination of the in situ state of stress has also been attacked vigorously (see Ref. [2] for a complete treatment). However, little attention has been paid to the estimation of boundary conditions for (numerical) models of rock masses at the engineering scale.

According to the classification presented in Fig. 2, the Bayesian procedures presented in this paper are to be considered as identification procedures.

3. Estimation of boundary conditions for a linearly elastic rock mass

3.1. Linear model

Consider a model $\mathfrak{M}$ of a rock mass featuring m boundary conditions X_i. Each boundary condition X_i can be either a displacement or a stress component

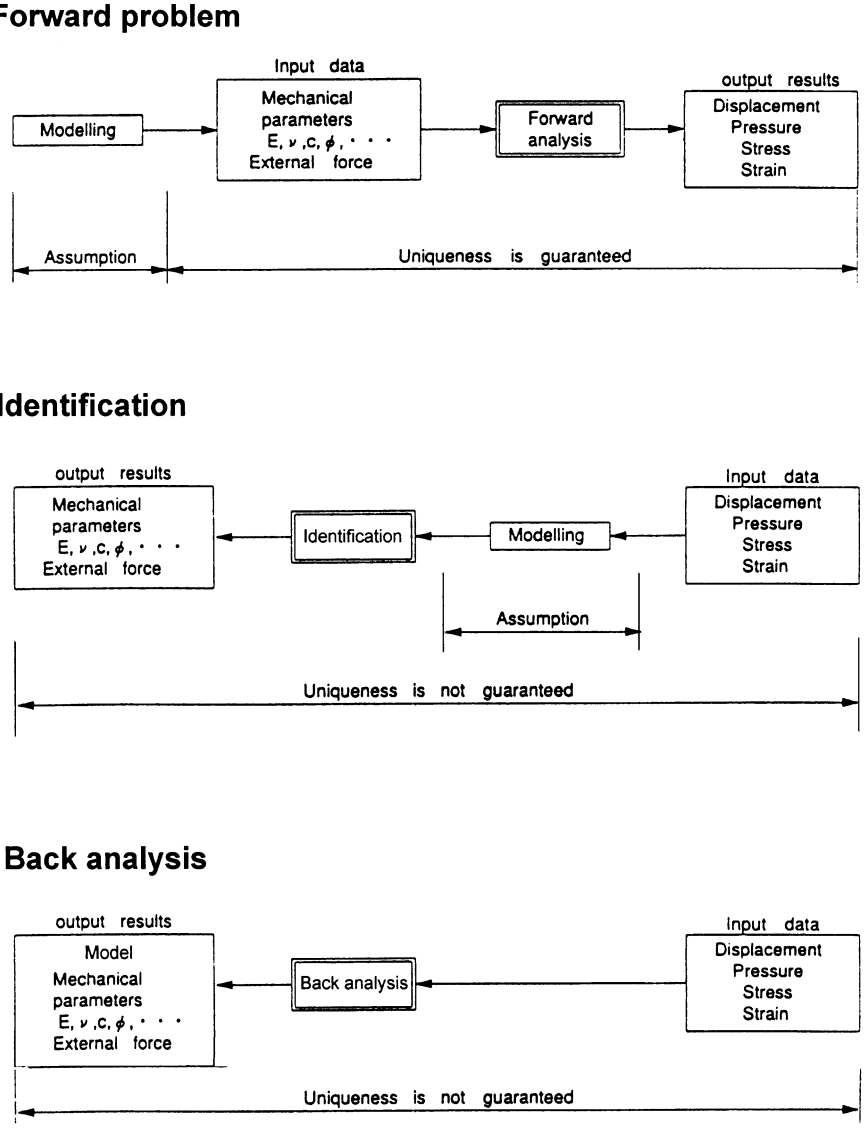

Fig. 2. Comparison between the procedures of forward analysis, identification, and back analysis (modified after Ref. [14]).

applied to a portion of $\mathfrak{M}$. Let us assume that $n \geqslant m$ measurements Z_i are available. To illustrate, let Z_i be a stress component measured at a point P, say $\sigma_{st}(P)$. Let W_i be the stress component $\sigma_{st}(P)$ calculated by means of $\mathfrak{M}$ when only gravity is acting, and all boundary conditions are set equal to zero, i.e. $X_i = 0$, $i = 1, \ldots, m$. Let us define:

$$Y_i = Z_i - W_i, \tag{1}$$

$$Y = (Y_1, \ldots, Y_n)^{\mathrm{T}}, \tag{2}$$

where a superscript "T" indicates a transpose vector.

If a unit boundary condition X_j is applied, all other boundary conditions being equal to zero and gravity being absent, a value of the stress component $y_j = \sigma_{st}{}^*(P)$ can be calculated by means of model $\mathfrak{M}$; let $h_{ij} := \sigma_{st}{}^*(P)$. If the rock mass is linearly elastic (it can be anisotropic and/or non-homogeneous) the superposition principle for linear elasticity holds [19], and, in general

$$y_i = \sum_{j=1}^{m} h_{ij} x_j \tag{3}$$

or, in matrix form:

$$Y = \mathbf{H}X, \tag{4}$$

where $\mathbf{H}$ is an $n \times m$ matrix, whose (i,j)th entry is h_{ij}.

Because some errors exist both in the measurements and in the model $\mathfrak{M}$, Eq. (4) must be modified as:

$$Y = \mathbf{H}X + U, \tag{5}$$

where U is an error vector of random variables. Vector U represents all errors involved, and has zero mean, covariance matrix $\mathbf{V}$, and is uncorrelated with X (see Eqs. (A.14a)–(A.14c)). It is also assumed that a priori information on boundary conditions X is available, and that such information is condensed in the mean matrix μ_X and covariance matrix $\mathbf{V}_{XX}$ given by Eqs. (A.11) and (A.12), respectively, i.e.

$$\mu_X := \mathbf{E}[X]$$

$$\mathbf{V}_{XX} := \mathbf{E}\left[\left(X-\mu_X\right)\left(X-\mu_X\right)^{\mathrm{T}}\right].$$

Since Eq. (5) is identical to Eq. (A.13), the Gauss–Markov theorem presented in the Appendix can be used to estimate the boundary conditions, by combining observational data and judgmental information, as is apparent from Eqs. (A.19), (A.20) and (A.21). More explicitly, according to the Gauss-Markov theorem, the best estimate of the boundary conditions is:

$$\hat{X} = \mu_X + \mathbf{A}^*(Y - \mathbf{H}\mu_X),$$

where

$$\mathbf{A}^* = \mathbf{V}_{XX}\mathbf{H}^{\mathrm{T}}(\mathbf{H}\mathbf{V}_{XX}\mathbf{H}^{\mathrm{T}} + \mathbf{V})^{-1}.$$

The determination of matrix $\mathbf{H}$ is conceptually similar to the first step in the UET procedure described in Section 2. However, here no restriction is made on the model $\mathfrak{M}$, provided it is linearly elastic. The application of the Gauss–Markov theorem is conceptually similar to the second step in the UET procedure. However, in contrast to a least-squares approach, the Bayesian approach allows for the combination of different sources of information, and for information updating as well.

The structure of matrix $\mathbf{H}$ sheds light on the nature of the problem under consideration. The following cases can occur:

(a) If the rank of matrix $\mathbf{H}$ is m, and $n > m$, then the problem is overdetermined, i.e. there are more data points than model parameters to be fitted. In general, there exists no solution that satisfies all simultaneous equations in Eq. (5), and an optimality criterion must be introduced in order to identify a solution. There will be as many solutions as many optimality criteria. Here, the optimality criterion is the minimization of $\mathbf{Q}$ in Eq. (A.16b).
(b) If the rank of matrix $\mathbf{H}$ is m, and $n = m$, then the problem is evendetermined, i.e. there are as many data points as many model parameters to be fitted. In this case, if the problem is deterministic, the solution is simply obtained by inverting matrix $\mathbf{H}$.
(c) If the rank of matrix $\mathbf{H}$ is less than m, then the problem is underdetermined, i.e. there are less data points than model parameters to be fitted. In general, there exist infinite solutions that satisfy all simultaneous equations in Eq. (5).

In practical applications, case (a) is to be preferred because of measurement errors and model limitations. In the following, the problem is assumed to be overdetermined [12].

3.2. Numerical examples

In order to understand the meaning of the proposed model, simple synthetic applications will be studied, in which only two boundary conditions are involved. Example 1 shows the effect of uncertainty affecting measurements, Example 2 shows the effect of additional measurements, Example 3 shows the effect of measurement errors, and Example 4 shows an application to a realistic topography.

3.2.1. Example 1

Consider a parallelepiped as in Fig. 3, in which displacements along the x-axis are prevented for points on face OCGH, displacements along the y-axis are prevented for points on face DHGF, and displacements along the z-axis are prevented for points on face OADH. Two uniform boundary normal stresses are applied on faces ABFD and OABC, and are denoted as X_1 and X_2, respectively.

Let us suppose that only two stress measurements are carried out at a point P: one to measure σ_{xx} and one to measure σ_{yy}. Moreover, let us suppose that the real applied boundary stresses are equal to 1 MPa. Evidently, one will measure $Z_1 = \sigma_{xx} = 1\,\mathrm{MPa}$ and $Z_2 = \sigma_{yy} = 1\,\mathrm{MPa}$ at any point of the rock mass; the computed stresses due to gravity are zero, i.e. $W = (0,0)^{\mathrm{T}}$. From Eq. (1) one obtains:

$$Y = Z - W = \begin{pmatrix}1\\1\end{pmatrix} - \begin{pmatrix}0\\0\end{pmatrix} = \begin{pmatrix}1\\1\end{pmatrix}\mathrm{MPa}. \tag{6}$$

Matrix $\mathbf{H}$ reads:

$$\mathbf{H} = \begin{pmatrix}1 & 0\\ 0 & 1\end{pmatrix}. \tag{7}$$

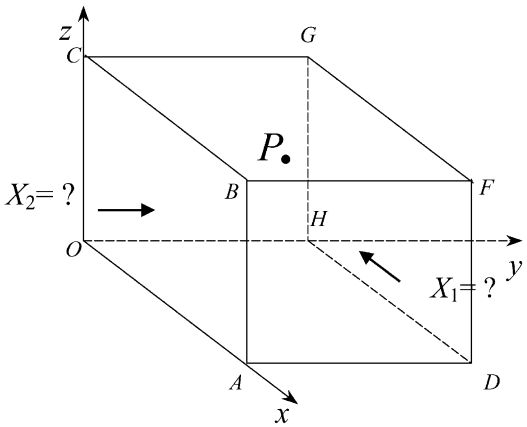

Fig. 3. Portion of a rock mass with flat topography and applied normal stresses on the boundary.

It is assumed that the a priori information is as follows: "the normal horizontal stresses are between 0.5 and 2 MPa". Within Probability Theory and according to the maximum entropy principle [20–22], a uniform distribution between 0.5 and 2 MPa must be adopted. Therefore, the a priori distribution functions are:

$$p_i^0(x_i) = \begin{cases} \dfrac{1}{2-0.5} = \dfrac{2}{3} & \text{for } 0.5 \leqslant x_i \leqslant 2\,\text{MPa} \\ 0 & \text{Otherwise} \end{cases}. \tag{8}$$

Eqs. (A.11) and (A.12) yield:

$$\mu_X = \mathbf{E}[X] = \begin{pmatrix} 1.25 \\ 1.25 \end{pmatrix}. \tag{9}$$

$$V_{XX} = \mathbf{E}[(X-\mu_X)(X-\mu_X)^{\mathrm{T}}] = \begin{pmatrix} 0.185 & 0 \\ 0 & 0.185 \end{pmatrix}. \tag{10}$$

As far as the error is concerned, all measurements are assumed to be affected by the same dispersion and the associated errors are assumed to be uncorrelated [15]. Thus:

$$\mathbf{V} = \sigma^2 \mathbf{I}, \tag{11}$$

where σ^2 is the variance of all measurements, and $\mathbf{I}$ is the identity matrix. A coefficient of variation equal to 0.2 is assumed, which yields $\sigma = 0.2$ MPa. By applying the Gauss–Markov theorem to these data, one obtains:

$$\mathbf{A}^* = \begin{pmatrix} 0.5395 & 0 \\ 0 & 0.5395 \end{pmatrix}. \tag{12}$$

$$\hat{X} = (1.1151, 1.1151)^{\mathrm{T}}. \tag{13}$$

Fig. 4a shows the values of the estimators $\hat{X}_1$ and $\hat{X}_2$ versus the value of the standard deviation of the error σ. The two estimators always coincide and, when $\sigma = 0$ (no uncertainty on the measurements), the estimators are equal to those obtainable if the problem were deterministic, and no a priori information were available, i.e. from Eq. (A.13):

$$X = Y\mathbf{H}^{-1} = \begin{pmatrix} 1 \\ 1 \end{pmatrix}. \tag{14}$$

3.2.2. Example 2

The same example as in Example 1 is considered. In addition to the two stress measurements, a strain measurement along the y-axis is also assumed to be available. If the Young's modulus is 10 MPa, matrix $\mathbf{H}$ is:

$$\mathbf{H} = \begin{pmatrix} 1 & 0 \\ 0 & 1 \\ 0 & 0.1 \end{pmatrix} \tag{15}$$

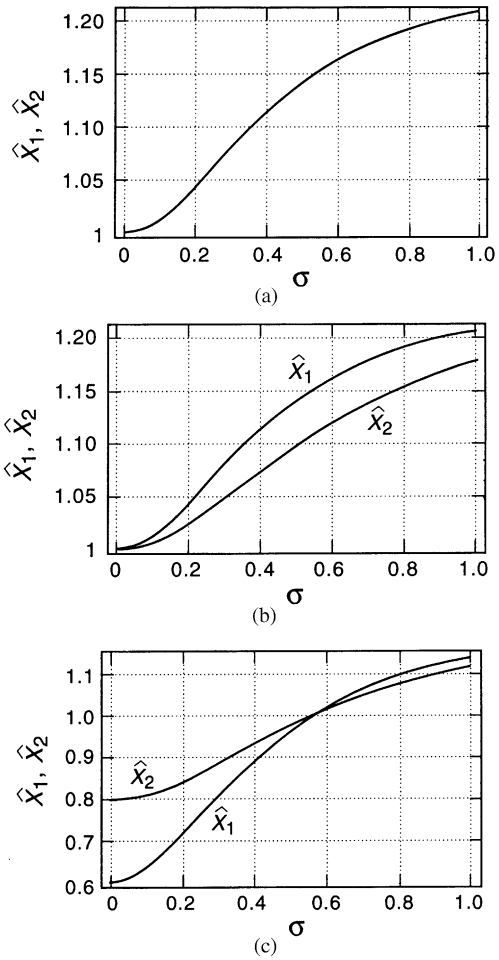

Fig. 4. Estimators for the boundary stresses (MPa) versus the value of the standard deviation of the error, σ (MPa). (a) Example 1; (b) Example 2; (c) Example 3.

and vector Y is:

$$Y = Z - W = \begin{pmatrix} 1 \\ 1 \\ 0.1 \end{pmatrix} - \begin{pmatrix} 0 \\ 0 \\ 0 \end{pmatrix} = \begin{pmatrix} 1 \\ 1 \\ 0.1 \end{pmatrix} \text{MPa}. \tag{16}$$

The a priori information is the same as in Example 1. It is still assumed that errors are uncorrelated, and that all errors have the same coefficient of variation σ:

$$\mathbf{V} = \begin{pmatrix} 1 & 0 & 0 \\ 0 & 1 & 0 \\ 0 & 0 & 0.01 \end{pmatrix} \sigma^2. \tag{17}$$

Plotted in Fig. 4b are the values of the estimators $\hat{X}_1$ and $\hat{X}_2$ versus the value of the standard deviation of the error σ. Compared to Fig. 4a, the two estimators do not coincide except for $\sigma = 0$. In the latter case, the estimators are equal to the values in Eq. (14). The structure of matrix $\mathbf{H}$ in Eq. (15) tells us that the additional piece of information (i.e. the strain measurement) is related only to X_2. Thus, the estimated values

for X_1 are the same as those in Example 1 (see Fig. 4a). On the contrary, the estimated values for X_2 benefit by the additional information because they are less sensitive to the a priori information, even when large uncertainty affects the updating information. This means that, the more updating information is collected, the heavier its weight will be on the estimation of the boundary conditions.

3.2.3. Example 3

In this example, the effect of errors in the measured values is investigated. It is assumed that, all the rest being identical to Example 2, the measured stresses at P are both equal to 0.6 MPa (i.e. they are different from the "true" value of 1 MPa), while the measured strain is correct and equal to 0.1. The results are portrayed in Fig. 4c. By comparing Figs. 4c and 4b, it appears that the values of the estimators are very much affected by the wrong measurements. Since only one piece of information is available on X_1, its estimator is visibly wrong for low values of σ, i.e. when it is believed that the measurement error is small. This effect is mitigated for the estimator of X_2 by the presence of another (exact) measurement. When $\sigma = 0$, the estimator $\hat{X}_2 = 0.8$ MPa is the average between the estimators one would obtain with the only stress measurement (i.e. $\hat{X}_2 = 0.6$ MPa) and the only strain measurement (i.e. $\hat{X}_2 = 1$ MPa). For large values of the error, the observations in Example 2 apply, i.e. the presence of a second measurement decreases the importance of the a priori information.

3.2.4. Example 4

Consider the rock mass model of Fig. 5a. Compared to the previous examples, the rock mass has an irregular topography consisting of a series of ridges and valleys. The displacements along the x-axis are prevented for points on face OCGH, the displacements along the y-axis are prevented for points on face DHGF (i.e. planes OCGH and DHGF are vertical planes of symmetry), and the displacements along the z-axis are prevented for points on face OADH. Two uniform boundary normal stresses are applied to faces ABFD and OABC, and are denoted as X_1 and X_2, respectively. The calculations described in this section were carried out by means of the Finite Element program Strand7 [23]. The rock mass is assumed to be homogeneous, isotropic and linearly elastic.

The "real" applied boundary stresses are $x_1 = 1.5$ MPa and $x_2 = 5.2$ MPa.

It is assumed that the *a priori* information is the same as in Examples 1–3, i.e. "the horizontal stress is between 1 and 2 MPa. " As a consequence, the mean and the covariance matrix are given by Eqs. (9) and (10), respectively. It is to be noted that the actual value of the first boundary condition ($x_1 = 1.5$ MPa) is consistent with the a priori information, whereas the actual value of the second boundary condition ($x_2 = 5.2$ MPa) is well outside the a priori information range.

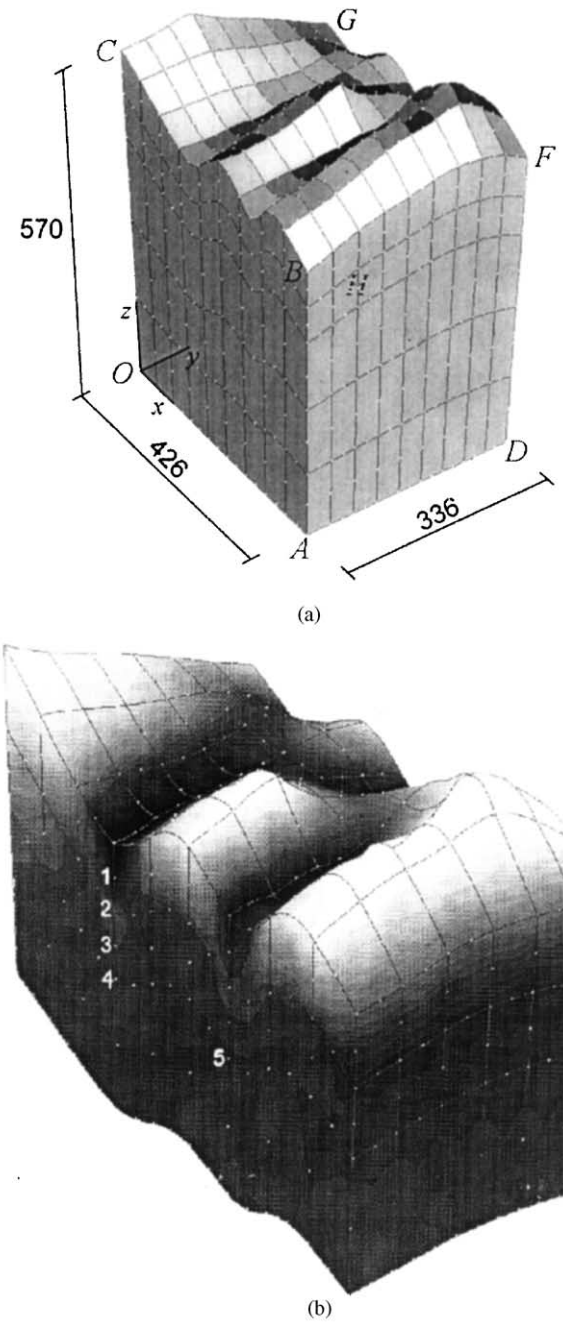

Fig. 5. (a) FEM model for Example 4, 20-node brick elements were used; (b) section of model for Example 4 showing the points at which the stress measurements are taken. Dimensions in meters.

As for in situ measurements, five measurements for σ_{xx} and σ_{yy} are carried out in two valleys at points 1 to 5, as shown in Fig. 5b. The values given in Table 1 have been obtained by subtracting the gravity effect from the actual measured values, according to Eq. (1).

Table 1
Observed vector $Y = (y_1, \ldots, y_{10})^T$ for Example 4

Point	σ_{xx} (MPa)	σ_{yy} (MPa)
1	$y_1 = 1.45313$	$y_2 = 4.87308$
2	$y_3 = 1.38263$	$y_4 = 5.07660$
3	$y_5 = 1.28404$	$y_6 = 4.88838$
4	$y_7 = 1.09634$	$y_8 = 4.66655$
5	$y_9 = 1.75178$	$y_{10} = 4.93349$

All measurements are given the same coefficient of variation COV = 0.2, and their errors are assumed to be uncorrelated. The non-zero elements of the diagonal covariance matrix **V** of the error are as follows (in MPa^2):

$$V(1,1) = 0.0844 \quad V(2,2) = 0.9499$$
$$V(3,3) = 0.0765 \quad V(4,4) = 1.0309$$
$$V(5,5) = 0.0659 \quad V(6,6) = 0.9558$$
$$V(7,7) = 0.0481 \quad V(8,8) = 0.8711$$
$$V(9,9) = 0.1227 \quad V(10,10) = 0.9736,$$

where, in general:

$$V(i,i) = (y_i \, \mathrm{COV})^2$$

y_i = observed stress (see Table 1).

As for matrix **H**, a unit pressure is first applied to face ABFD, and face OABC is left stress-free (see Fig. 5a): the entry $h_{(2i-1),1}$ is the calculated stress σ_{xx} at point i, the entry $h_{(2i),1}$ is the calculated stress σ_{yy} at point i. Then, a unit pressure is applied to face OABC, and face ABFD is left stress-free (see Fig. 5a): the entry $h_{(2i-1),2}$ is the calculated stress σ_{xx} at point i, the entry $h_{(2i),2}$ is the calculated stress σ_{yy} at point i. Matrix **H** is:

$$\mathbf{H} = \begin{pmatrix} 0.9578 & 0.0024 & 0.9180 & 0.0029 & 0.8622 & 0.0006 & 0.7752 & 0.0010 & 1.2822 & 0.1476 \\ 0.0031 & 0.9364 & 0.0010 & 0.9754 & 0.0018 & 0.9402 & 0.0128 & 0.8971 & 0.0329 & 0.9062 \end{pmatrix}^T.$$

Application of the Gauss–Markov theorem yields:

$$\mathbf{A}^* = \begin{pmatrix} 0.1761 & 0.0006 & 0.1864 & 0.0006 & 0.2030 & 0.0006 & 0.2502 & 0.0006 & 0.1620 & 0.0029 \\ 0.0105 & 0.0997 & 0.0086 & 0.0957 & 0.0051 & 0.0995 & -0.0172 & 0.1042 & -0.0290 & 0.0943 \end{pmatrix}.$$

$$\hat{X} = (1.467, 3.067)^T.$$

The in situ measurements almost confirmed the a priori value of X_1 because the a posteriori estimate is 17% higher than the a priori mean for X_1. However, the in situ measurements made the a posteriori estimate for X_2 increase dramatically by 145%.

4. Estimation of boundary conditions for a non-linear model

4.1. Augmented secant procedure

Consider the case in which, due to material non-linearities of model $\mathfrak{M}$, the kth measured quantity (stress, strain, or displacement) is a non-linear function, z_k, of the boundary conditions:

$$z_k = z_k(x_1, x_2, \ldots, x_m). \tag{18}$$

Because of material non-linearities, the model response is path-dependent. For example, different results are obtained if the boundary conditions are applied simultaneously, or at different stages following a specific order. In this paper, it is assumed that all boundary conditions are applied simultaneously to the model.

Obtaining a closed-form expression for the derivatives of z_k is generally not possible, because the model in hand is a numerical model. Finite differences or perturbation theory could be used, but the authors have found that a secant approach is more robust and allows the computer runs of model $\mathfrak{M}$ to be minimized. It is believed that minimizing computer runs is the crucial point when the rock mass model $\mathfrak{M}$ is complex. An iterative scheme is thus proposed, in which at every step a linear estimation problem is solved. The Gauss–Markov theorem mentioned in the Appendix is used to solve the linearized problem.

To illustrate, let us consider the case of two boundary conditions, the extension to more than two variables being straightforward. If there is no interaction between x_1 and x_2, and z_k is zero for $(x_1, x_2) = (0, 0)$, one can write:

$$z_k = h_{k1}(x_1)x_1 + h_{k2}(x_2)x_2. \tag{19}$$

In an iterative setting, let (x_1^{j-1}, x_2^{j-1}) be the value of X available at the jth iteration. If there is interaction between x_1 and x_2, and/or z_k is not equal to zero for $(x_1, x_2) = (0, 0)$, one can force the linear approximation $h_{k1}^j x_1 + h_{k2}^j x_2$ to pass through the point

$\xi_k^j := z_k(x_1^{j-1}, x_2^{j-1})$. Let:

$$\zeta_k^j := h_{k1}^j x_1^{j-1} + h_{k2}^j x_2^{j-1}. \tag{20}$$

From the identity:

$$\xi_k^j - (\xi_k^j - \zeta_k^j) = h_{k1}^j x_1^{j-1} + h_{k2}^j x_2^{j-1},$$

valid for a generic point (x_1, x_2), the following approximation holds:

$$z_k - (\xi_k^j - \zeta_k^j) \approx h_{k1}^j x_1 + h_{k2}^j x_2. \tag{21}$$

Introducing the observed value y_k, it follows that:

$$y_k - (\xi_k^j - \zeta_k^j) \approx h_{k1}^j x_1 + h_{k2}^j x_2. \tag{22}$$

The left-hand side of Eq. (22), $y_k^j = y_k - (\xi_k^j - \zeta_k^j)$, becomes a new observable random variable, similar to y_k in the linear model described above in Section 3.1.

Thus, the iterative procedure can be outlined as follows (if $j = 1$, the a priori mean value may be used, i.e. $(x_1^0, x_2^0) = \mu_X$) [24–26]:

(i) By calculating $z_k(x_1^{j-1}, 0)$, the secant value:

$$h_{k1}^j = z_k(x_1^{j-1}, 0)/x_1^{j-1} \tag{23}$$

is obtained. Similarly, by calculating $z_k(0, x_2^{j-1})$, the secant value $h_{k2}^j = z_k(0, x_2^{j-1})/x_2^{j-1}$ is obtained.

(ii) Calculate

$$\xi_k^j = z_k(x_1^{j-1}, x_2^{j-1}), \tag{24a}$$

$$\zeta_k^j = h_{k1}^j x_1^{j-1} + h_{k2}^j x_2^{j-1}, \tag{24b}$$

$$y_k^j = y_k - (\xi_k^j - \zeta_k^j). \tag{24c}$$

(iii) The Gauss–Markov theorem described in the Appendix with the new augmented observables y_k^j and matrix components h_{ki}^j can be used to calculate a new estimate of the boundary conditions $\hat{X}^j = (x_1^j, x_2^j)$ by means of Eqs. (A.19) and (A.21).

(iv) Go to point (i) unless the relative error:

$$R^j = \sqrt{\sum_k^n \left(\xi_k^{j+1} - y_k\right)^2 / \sum_k^n (y_k)^2} \tag{25}$$

is less than a specified value or a maximum number of iterations has been achieved.

The a priori information embodied in μ_X and V_{XX} must not be changed during the iterative process because the iterative process is only aimed at finding the correct linearization of the problem and does not add any new piece of information.

The proposed procedure can be interpreted geometrically as follows. In the (x_1, x_2, y_k) space, at the jth step, the surface $y_k = z_k(x_1, x_2)$ is approximated by a plane α passing through point, $P_k^j = (0, 0, \xi_k^j - \zeta_k^j)$, and orthogonal to vector $\mathbf{u} = (h_{k1}^j, h_{k2}^j, -1)$. In fact, for any point $P = (x_1, x_2, y_k)$ belonging to α, vector PP_k^j must satisfy the following scalar equation:

$$P_k^j P \cdot \mathbf{u} = 0$$

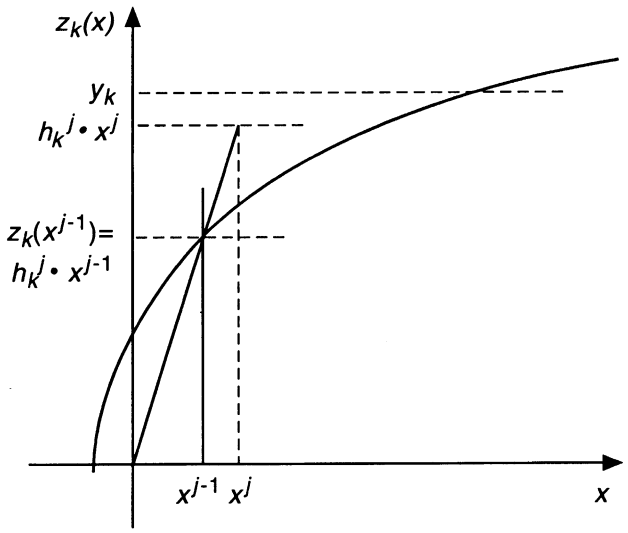

Fig. 6. Successive iterations for the non-linear procedure with one boundary condition ($m = 1$).

i.e.:

$$h_{k1}^j x_1 + h_{k2}^j x_2 - (y_k - (\xi_k^j - \zeta_k^j)) = 0$$

and:

$$y_k - (\xi_k^j - \zeta_k^j) = h_{k1}^j x_1 + h_{k2}^j x_2.$$

The latter equation is equal to Eq. (22).

A graphical interpretation in shown in Fig. 6, for the case of one boundary condition only ($m = 1$). In this later case, ξ_k^j (defined in Eq. (24a)) coincides with ζ_k^j (defined in Eq. (24b)), and Eq. (24c) becomes:

$$y_k^j = y_k - (\xi_k^j - \zeta_k^j) = y_k = \text{const.} \tag{26}$$

Thus, when $m = 1$, the procedure resembles a classical secant method. However, as can be seen in Fig. 6, in general, $h_k^j x^j \neq y_k$ whenever the problem is overdetermined. This is because in an overdetermined problem (loosely speaking "more data points than model parameters to be fitted"), it is not possible to find a solution that satisfies exactly all data points.

4.2. General procedure

An extensive numerical investigation carried out by means of elasto-plastic models (either perfectly plastic or softening) has revealed the following fact [24]. When both of the following two conditions occur:

(a) The boundary conditions $\hat{X}^{j-1} = (x_1^{j-1}, x_2^{j-1})$ are such that the relative error R^{j-1} in Eq. (25) is greater than 100%.

(b) The measured stresses, displacements or strains are smaller than the calculated ones, i.e.

$$\xi_k^j - y_k > 0, \quad k = 1, \ldots, n. \tag{27}$$

Then $\xi_k^j \gg \zeta_k^j$, and y_k^j in Eq. (24c) becomes meaningless. As a result, the iterative procedure may not converge. In this case, a simple secant approach proved to be the most effective procedure. Then, Eq. (24c) is replaced by:

$$y_k^j = y_k. \tag{24c*}$$

In the following, this procedure will be referred to as the "simple secant method", whereas the procedure presented in Section 4.1 will be referred to as the "augmented secant method".

To summarize, the iterative procedure is as follows:

(i) By calculating $z_k(x_1^{j-1}, 0)$, the secant value:

$$h_{k1}^j = z_k(x_1^{j-1}, 0)/x_1^{j-1} \tag{28}$$

is obtained. Similarly, by calculating $z_k(0, x_2^{j-1})$, the secant value $h_{k2}^j = z_k(0, x_2^{j-1})/x_2^{j-1}$ is obtained.

(ii) Calculate:

$$\zeta_k^j = h_{k1}^j x_1^{j-1} + h_{k2}^j x_2^{j-1}. \tag{29}$$

If $j = 1$, Calculate:

$$\xi_k^1 = z_k(x_1^0, x_2^0)$$

$$R^0 = \sqrt{\sum_k^n (\xi_k^1 - y_k)^2 / \sum_k^n (y_k)^2}.$$

(iii) If both conditions (a) and (b) above occur, then use the simple secant method:

$$y_k^j = y_k \tag{30a}$$

else, use the augmented secant method:

$$y_k^j = y_k - (\xi_k^j - \zeta_k^j). \tag{30b}$$

(iv) The Gauss–Markov theorem, mentioned in the Appendix, with the observables y_k^j and matrix components h_{ki}^j can be used to calculate a new estimate of the boundary conditions $\hat{X}^j = (x_1^j, x_2^j)$ by means of Eqs. (A.19) and (A.21).

(v) Calculate:

$$\xi_k^{j+1} = z_k(x_1^j, x_2^j). \tag{31}$$

(vi) Go to point (i) unless the relative error:

$$R^j = \sqrt{\sum_k^n (\xi_k^{j+1} - y_k)^2 / \sum_k^n (y_k)^2} \tag{32}$$

is less than a specified value or a maximum number of iterations has been achieved.

4.3. Comparison with the identification procedure proposed by Cividini et al. (1983)

The Gauss–Markov theorem was also used by Cividini et al. [15]. They consider a linearly elastic rock mass with Young's modulus E_1, and a lens of different material (inclusion) with Young's modulus E_2. Known loads are applied to the rock mass surface, and the induced surface displacements are measured. The objective is to estimate the elastic moduli E_1 and E_2, and the parameters governing the geometry of the inclusion. Because the measured displacements depend on the model parameters in a non-linear fashion, an iterative procedure is proposed, which is similar to the procedures put forward by other scholars (e.g. Refs. [27–30]).

According to these procedures, at the jth step, matrix $\mathbf{H}^j$ is treated as a sensitivity matrix, and is calculated by means of finite difference approximations as follows:

$$h_{k1}^j = z_k(x_1^{j-1} + \mathrm{d}x_1, x_2^{j-1}) - z_k(x_1^{j-1}, x_2^{j-1});$$

$$h_{k2}^j = z_k(x_1^{j-1}, x_2^{j-1} + \mathrm{d}x_2) - z_k(x_1^{j-1}, x_2^{j-1}).$$

However, the following problems arise when these procedures are applied to the estimation of the boundary conditions:

(a) Increment $\mathrm{d}x_i$ must depend on the curvature of the curve $(x_i, z_k(x_i))$. Thus, an adaptive algorithm must be introduced, whose robustness cannot be guaranteed for general applications.

(b) If the first derivative $\mathrm{d}z_k/\mathrm{d}x_i$ is zero in a neighborhood of x_i^j, then $h_{ki}^j = 0$ (see Fig. 7a), and the ith boundary condition has no effect on the kth measurement. Consequently, the redundancy of the measurements is reduced. As a limiting case, the problem may become underdetermined, and thus the iterative procedure may fail. This happens, for example, if $h_{ki}^j = 0$, $k = 1, \ldots, n$, because in this case the rank of matrix $\mathbf{H}^j$ becomes equal to $m - 1$.

On the contrary, the iterative scheme proposed in Section 4.2 does not suffer from these problems, as sketched in Fig. 7b for the case of one boundary condition only.

4.4. Limitations of the proposed iterative procedure

The iterative procedure proposed in Section 4.2 presents the following limitations:

(a) The procedure fails when $x_j^{i-1} = 0$ because, in this case, the ratio in Eq. (28) is meaningless. However,

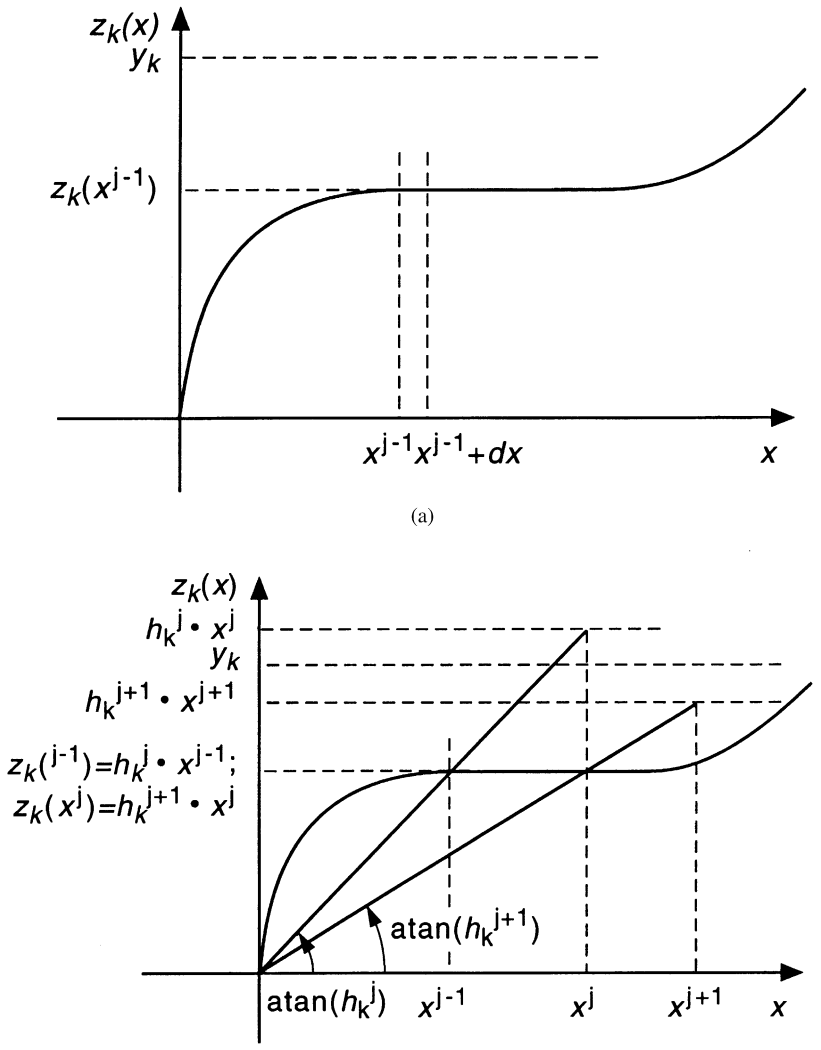

Fig. 7. Comparison between: (a) the iterative scheme proposed by Cividini et al. [15], and (b) the iterative scheme proposed in Section 4.2. For simplicity, the case of one boundary condition only is portrayed. In Fig. 7b, because $z_k(x^{j-1}) = z_k(x^j)$, and $x^{j-1} < x^j$, from Eq. (28) it turns out that: $h_k^{j+1} = z_k(x^j)/x^j < h_k^j = z_k(x^{j-1})/x^{j-1}$.

in practice, this limitation can be overcome by using a small value for x_i^{j-1} in Eq. (28).

(b) The procedure fails at step (i) in Section 4.2, if no solution exists for the boundary conditions $y = (0, \ldots, x_i^{j-1}, \ldots, 0)$, i.e. if the function $z_k(0, \ldots, x_i^{j-1}, \ldots, 0)$ is undefined. Consider, for example, a triaxial test, in which the unknown boundary conditions are the confining (cell) pressure, X_1, and the deviator stress, X_2. If the soil is cohesionless, the specimen fails under the boundary conditions $x_1 = 0, x_2 > 0$.

(c) Because of the non-linearity of the problem, multiple solutions may exist. This is typical of ill-posed identification problems. In these cases, the procedure proposed may show no convergence, but a rather oscillating behavior. This topic was dealt with by the authors in Ref. [31], and illustrated by means of examples of ill-posed problems in tunnel monitoring.

5. Application to the Underground Research Laboratory

The Canadian nuclear waste disposal concept considers the plutonic rock of the Canadian Shield as a potential host medium for a disposal vault located between 500 and 1000 m depth. As part of the assessment of this concept, Atomic Energy of Canada Limited (AECL) has constructed an Underground Research Laboratory (URL) approximately 120 km northeast of Winnipeg, Manitoba, in the Lac du Bonnet granite batholith (Fig. 8).

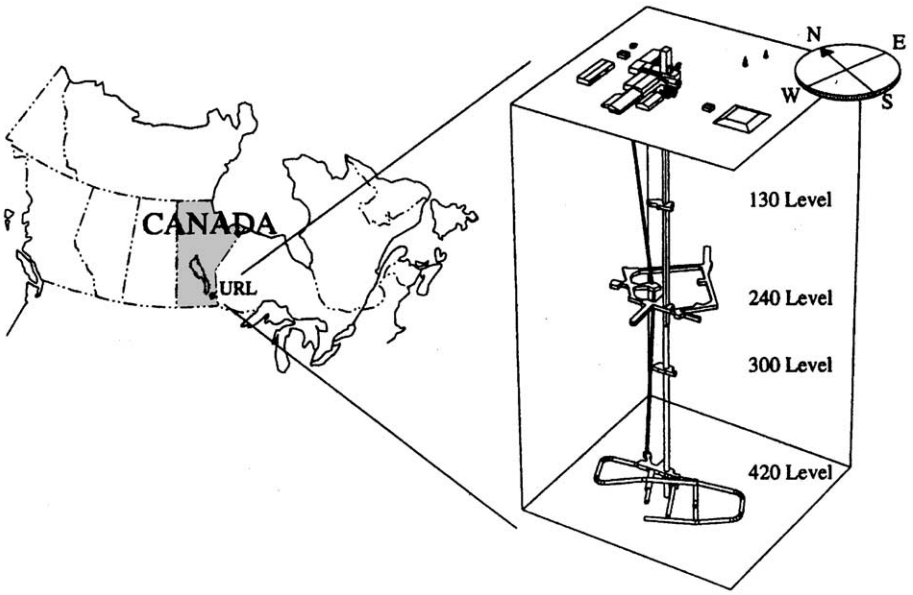

Fig. 8. Location and arrangement of AECL's Underground Research Laboratory showing the main working levels (after Ref. [62]).

The application to the URL site of the iterative procedure for boundary condition estimation considers as a priori information the stress data relative to the Canadian Shield gathered by Herget [35]. The updating information consists of the stress measurements conducted in over 15 years along and in the vicinity of the URL shaft [36].

5.1. Geologic setting

5.1.1. Regional setting

The URL is located within the Lac du Bonnet granite batholith (LDBB), which is considered to be representative of many granitic intrusions of the Precambrian Canadian Shield [37,38]. The batholith trends East–Northeast and its elongated body is about 75 by 25 km in surface area (Fig. 9), and extends to a depth of about 10 km. Dated as Late Kenoran age (2680 ± 81 Ma), the batholith lies in the Winnipeg River plutonic complex of the English River gneiss belt of the western Superior Province. The batholith is a relatively undifferentiated pink and grey massive porphyritic granite-granodiorite. The massive, medium-to-coarse-grained porphyritic granite is relatively uniform in texture and composition over the batholith, although locally it displays subhorizontal gneissic banding. Low-dipping thrust faults and associated systems of predominantly north-northeast striking subvertical joints occur throughout the LDBB.

The style of fracturing within the central portion of the LDBB near the URL is dominated by large, low-dipping thrust faults and splays. The blocks between the thrust faults are crosscut by one or more sets of subvertical joints, the pattern and frequency of which vary from one block (fracture domain) to the next. The factors influencing the pattern of intrablock jointing include the overall distance from the surface, the proximity to the bounding faults, and the local rock type. The subvertical joints become less frequent, less continuous and simpler in pattern with increasing depth.

5.1.2. Local setting

The local geologic setting was first determined by site investigations carried out from the surface. The location of the URL shaft was selected to provide a range of lithological and structural domains. Excavation of the URL shaft intersected two major thrust faults that dip about 25–30° southeast. These faults are referred to as Fracture Zone 3 and Fracture Zone 2, and the splays as Fracture Zones 2.5 and 1.9 (Fig. 10a). The fracture zones are composed of chloritic slip surfaces, which grade into cataclastic zones where displacements in the order of meters to tens of meters have occurred. The cataclastic zones range in thickness from 20 mm to 1 m and contain breccia and clay gouge. Where the URL shaft intersects Fracture Zone 2 there is 7.3 m of reverse displacement on Fracture Zone 2 [39]. These fracture zones are considered to be the main pathways for groundwater flow in the Lac du Bonnet batholith [40].

Between the surface and Fracture Zone 2.5, the rock is pink granite and contains a prominent subvertical joint set striking about 020° near the surface, to 040° at the 240 Level. A less prominent subvertical joint set strikes between 150° and 180°. The pink color is due to alteration by moving groundwater.

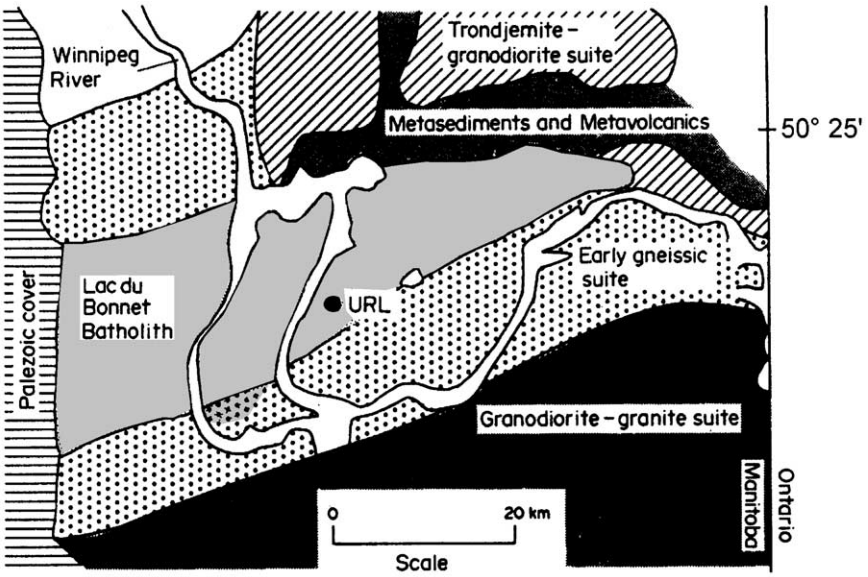

Fig. 9. Generalized geology of the Lac du Bonnet batholith (after Ref. [44]).

The general rock type below Fracture Zone 2.5 is a massive unjointed grey granite. Detailed geological mapping, however, has identified the following major rock types: xenolithic granite, leucocratic granite, fine-grained grey granite, and subvertical granodiorite and pegmatite dykes. In the immediate area of Fracture Zones 2 and 1.9 the grey granite shows pink alteration.

5.2. Rock mechanics properties

5.2.1. Laboratory characterization of intact rock

The mean and standard deviation of the uniaxial mechanical properties versus depth are summarized in Fig. 11 [41]. Within the upper 200 m (pink granite), the properties are relatively consistent with depth, but from 200 to 1000 m (grey granite) trends of decreasing compressive strength, longitudinal wave velocity and tangent modulus of elasticity with depth are evident.

This surprising trend can be explained if stress relief microcracking caused by the sampling process is considered [42]. Within the pink granite, the percentage of microcracks is about 16% of that found in the grey granite, and there is no significant increase in the percentage of microcrack porosity in the pink granite with depth. In the grey granite, however, the percentage of microcrack porosity increases with depth to about 20% of the total porosity (0.5%) of the grey granite samples at depths of about 400 m [43].

Geotechnical properties of rock samples measured at low confining stress are significantly affected by the volume of microcracks in the sample. This phenomenon is illustrated in Table 2 and Fig. 12a, showing the tangent Young's modulus of the pink and grey granite as a function of confining stress [43], and in Fig. 12b, showing the volumetric strain of the pink and grey granite as a function of axial stress. The behavior of the grey granite samples suggests that these samples experienced significant stress relaxation after drilling, resulting in higher crack porosity and, consequently, lower strength and higher deformability.

5.2.2. Joints and faults

Two groups of joint samples were tested in the laboratory [44]: samples of joints belonging to Fracture Zone 2 (Group 1) and the extensional set formed during the intrablock fracturing (Group 2). The samples were obtained from NQ (approximately 61 mm) cores. The results are given in Fig. 13. Joint Compressive Strength (JCS) and Joint Roughness Coefficient (JRC) values of Group 2 are higher and less dispersed than the corresponding values of Group 1.

By using the mean values for Group 1 (JCS = 70 MPa and JRC = 5), and assuming a residual friction angle, φ_r, equal to 30°, the tangent friction angle and apparent cohesion can be calculated following the procedure described by Mammino and Tonon [45]. A normal stress $\sigma_n^* = 0.027 \times 250 = 6.75$ MPa is assumed as representative of the vertical stress at a depth of 250 m, where Fracture Zone 2 intersects the URL shaft.

$$\left.\frac{\partial\tau}{\partial\sigma_n}\right|_{\sigma_n=\sigma_n^*=6.75} = \tan\left(\mathrm{JRC}_n \log_{10}\left(\frac{\mathrm{JCS}_n}{\sigma_n}\right) + \varphi_r\right) - \frac{\pi\,\mathrm{JRC}_n}{180\ln 10}\left\{\left[\tan\left(\mathrm{JRC}_n \log_{10}\left(\frac{\mathrm{JCS}_n}{\sigma_n}\right) + \varphi_r\right)\right]^2 + 1\right\} = 0.557. \quad (33)$$

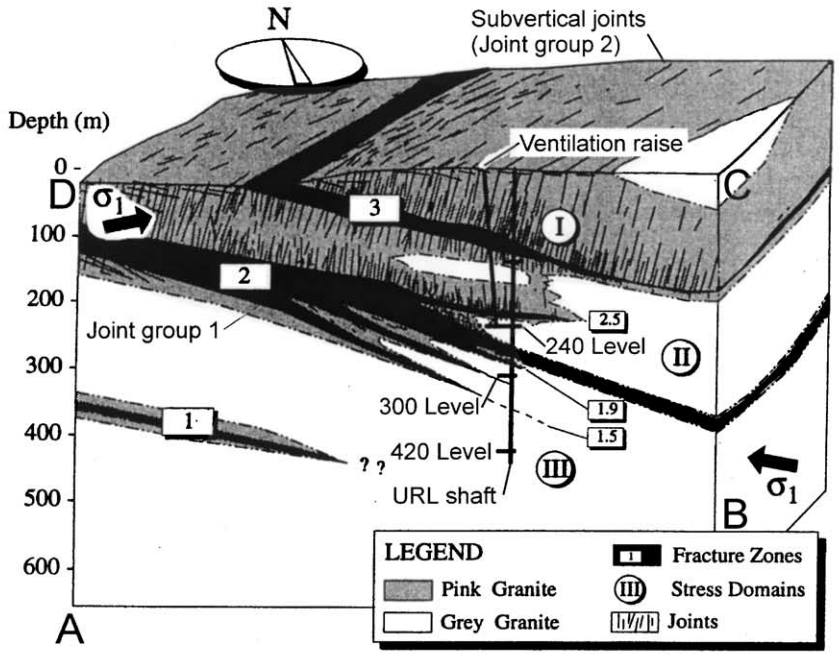
N
Subvertical joints
(Joint group 2)
Depth (m)
Ventilation raise
D
C
σ1
3
I
2
Joint group 1
2.5
240 Level
II
300 Level
1.9
1.5
1
? ?
420 Level
III
URL shaft
B
σ1
A
LEGEND
Pink Granite
Grey Granite
Fracture Zones
Stress Domains
Joints

(a)

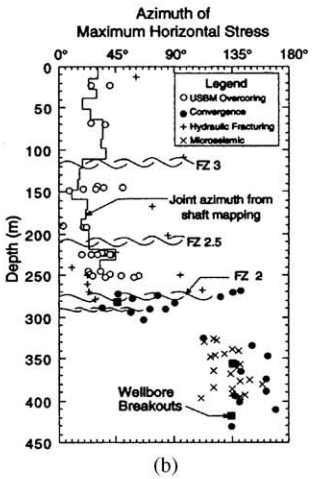
Azimuth of
Maximum Horizontal Stress
Legend
USBM Overcoring
Convergence
Hydraulic Fracturing
Microseismic
FZ 3
Joint azimuth from
shaft mapping
FZ 2.5
FZ 2
Wellbore
Breakouts
Depth (m)

(b)

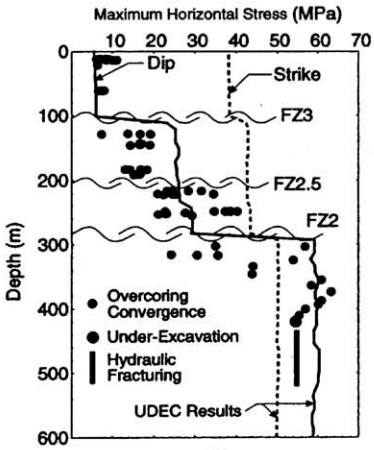
Maximum Horizontal Stress (MPa)
Dip
Strike
FZ3
FZ2.5
FZ2
Overcoring
Convergence
Under-Excavation
Hydraulic
Fracturing
UDEC Results
Depth (m)

(c)

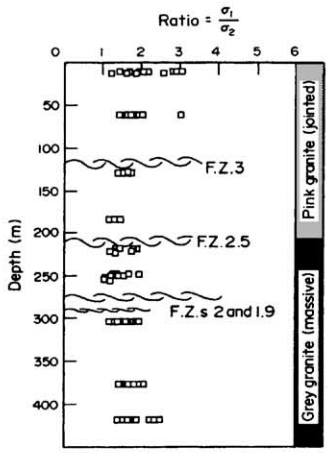
Ratio = σ1/σ2
F.Z.3
F.Z.2.5
F.Z.s 2 and 1.9
Pink granite (jointed)
Grey granite (massive)
Depth (m)

(d)

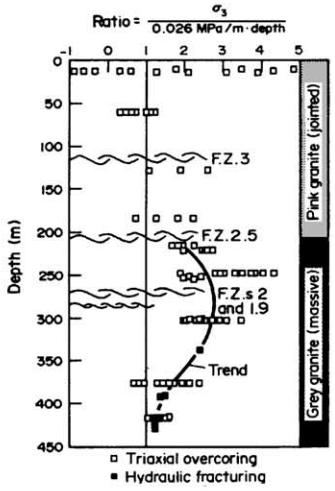
Ratio = σ3/0.026 MPa/m·depth
F.Z.3
F.Z.2.5
F.Z.s 2
and 1.9
Trend
Pink granite (jointed)
Grey granite (massive)
Depth (m)
Triaxial overcoring
Hydraulic fracturing

(e)

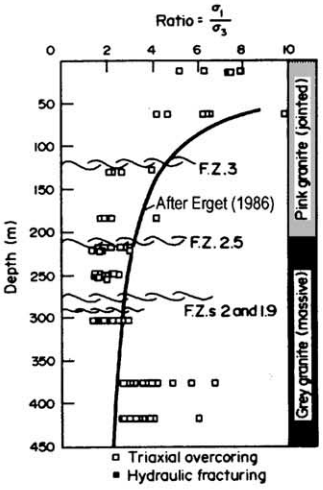
Ratio = σ1/σ3
F.Z.3
After Erget (1986)
F.Z.2.5
F.Z.s 2 and 1.9
Pink granite (jointed)
Grey granite (massive)
Depth (m)
Triaxial overcoring
Hydraulic fracturing

(f)

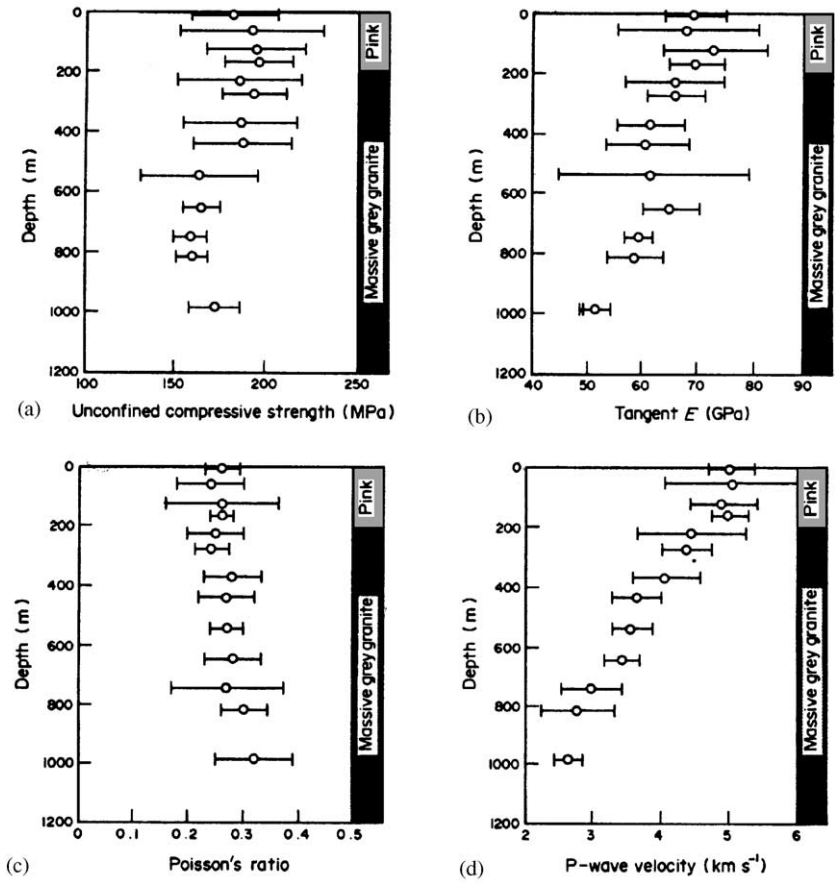

Fig. 11. (a–d) Unconfined mechanical properties versus depth of Lac du Bonnet granite laboratory samples (after Ref. [44]).

$$\varphi_i = \arctan\left(\frac{\partial\tau}{\partial\sigma_n}\right)\bigg|_{\sigma_n=\sigma_n*} = 30^\circ. \quad (34)$$

$$\tau^* = \sigma_n^* \tan\left(\mathrm{JRC}\log_{10}\left(\frac{\mathrm{JCS}}{\sigma_n^*}\right) + \varphi_r\right) = 4.74\,\mathrm{MPa}. \quad (35)$$

$$c_i = \tau* - \sigma_n \tan\varphi_i = 0.843\,\mathrm{MPa}. \quad (36)$$

However, three major problems arise in extrapolating these values to Fracture Zone 2:

(1) Because laboratory values are used, no allowance is made for scale effects in JRC and JCS [46].
(2) A representative value for the characteristic length of the discontinuity is difficult to identify in the thrust faults. This characteristic length is necessary in order to quantify scale effects.
(3) Fracture Zone 2 is composed of several joints (from which the laboratory specimens were taken), contains breccia and clay gouge, and underwent significant shear displacement (over 7 m in correspondence of the URL shaft).

For filled and sheared faults, a Coulomb failure criterion is generally preferred, with a typical friction angle of 20°, and zero cohesion [47].

In the present model, a constant shear stiffness $k_s = 30\,\mathrm{MPa/m}$ and a constant normal stiffness $k_n = 1000\,\mathrm{MPa/m}$ were assumed, based on published data [48–51] and numerical studies aimed to simulate the measured stress pattern.

5.2.3. Rock mass

The pink granite was thrust over the grey granite and along the weaker xenolithic layers followed by Fracture Zone 2. Because of the varying thickness of Fracture Zone 2, extension joints developed above

Fig. 10. (a) Geological setting of the Underground Research Laboratory showing the major fracture zones and stress domains (modified after Ref. [62]); (b) azimuth of maximum horizontal stress versus depth (the principal stress rotation below Fracture Zone 2 is evident), (after Ref. [36]); (c) maximum horizontal stress versus depth and results of UDEC distinct element models, (after Ref. [36]); (d) ratio of maximum over intermediate stress (both turn out to be horizontal) versus depth, (after Ref. [44]); (e) ratio of minor principal stress (vertical) to the calculated lithostatic stress, (after Ref. [44]); (f) ratio of maximum over minimum principal stress, the trend line is from Herget's database for the Canadian Shield (after Ref. [44]).

Table 2
Summary of laboratory geotechnical properties of Lac du Bonnet granite at the URL. (After ref. [44])

	Pink granite	Grey granite
Porosity (%)		
Range	0.16–0.28	0.32–0.67
Mean	0.24	0.50
Density (kg/m^3)		
Mean	2640	2630
Uniaxial compressive strength (MPa)		
Range	134–248	147–198
Mean	200	167
Brazilian tensile strength (MPa)		
Range	6.17–12.07	6.22–11.52
Mean	9.32	8.72
Tangent modulus (Gpa)		
Range	53–86	46–64
Mean	69	55
Poisson's ratio		
Range	0.18–0.44	0.13–0.43
Mean	0.26	0.3
Hoek and Brown failure parameters		
m	31.17	30.54
s	1	1

Fracture Zone 2, parallel to the strike of Fracture Zone 2. Consequently, an induced transverse isotropy has been created, whose vertical plane of symmetry is parallel to the strike of Fracture Zone 2. The rock mass Young's modulus parallel to the plane of transverse isotropy is assumed to be equal to the intact rock value determined in the laboratory, i.e. $E_1 = 60\,\text{GPa}$. The Young's modulus in direction orthogonal to the plane of transverse isotropy is assumed to be $E_2 = 30\,\text{GPa}$ [44]; this value is also equal to the Young's modulus in direction orthogonal the stress-relief induced micro-cracks measured in the laboratory (page 934 in Ref. [44]). A Young's modulus $E_2 = 30\,\text{GPa}$ corresponds to a Geological Strength Index (GSI) equal to [52]:

$$\text{GSI} = 40\log_{10}E_1 + 10 = 70. \tag{37}$$

The Poisson's ratios are assumed to be equal to 0.3. The shear modulus in planes orthogonal to the plane of transverse isotropy is calculated according to De Saint Venant formula [53]:

$$G_2 = \frac{E_2}{1 + 2\nu_2 + E_2/E_1} = 14\,\text{GPa}. \tag{38}$$

The absence of fractures in the grey granite leads us to assume an isotropic behavior for the grey granite, with Young's modulus $E = 60\,\text{GPa}$, and Poisson's ratio $\nu = 0.3$. In fact, although cored samples clearly display anisotropy, there is no evidence suggesting that anisotropy is significant in situ (page 929 in Ref. [44]). Also, in situ geophysical seismic surveys at the 240 Level in the grey granite indicate that shear wave velocities vary in different directions only by 5% (page 929 in Ref. [44]).

5.3. Measured in situ stresses

An extensive program of stress measurements has been implemented at the URL, and is summarized by Martino et al. [36]. The horizontal stresses can be grouped into three distinct stress domains, see Figs. 10a–f [54]. Horizontal stresses above Fracture Zone 2.5 are similar to the average stresses measured elsewhere in the Canadian Shield at similar depths [55]. Below Fracture Zone 2, the horizontal stresses measured at the URL are anomalously high compared to the average Canadian Shield stress, while the stresses

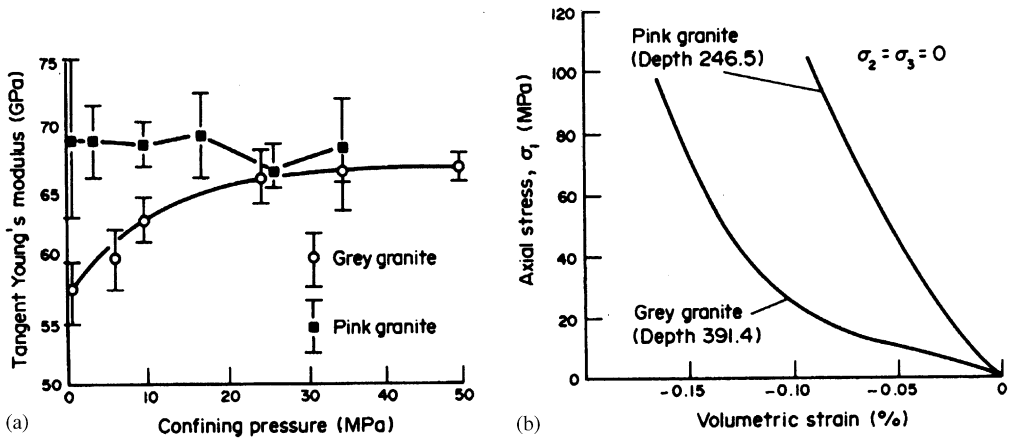

Fig. 12. (a) Tangent Young's modulus at 50% peak strength measured in triaxial compression tests on 45 mm diameter samples of Lac du Bonnet granite; (b) volumetric strains for the pink and grey granite under uniaxial loading (the non-linear response of the grey granite is evident) (after Ref. [44]).

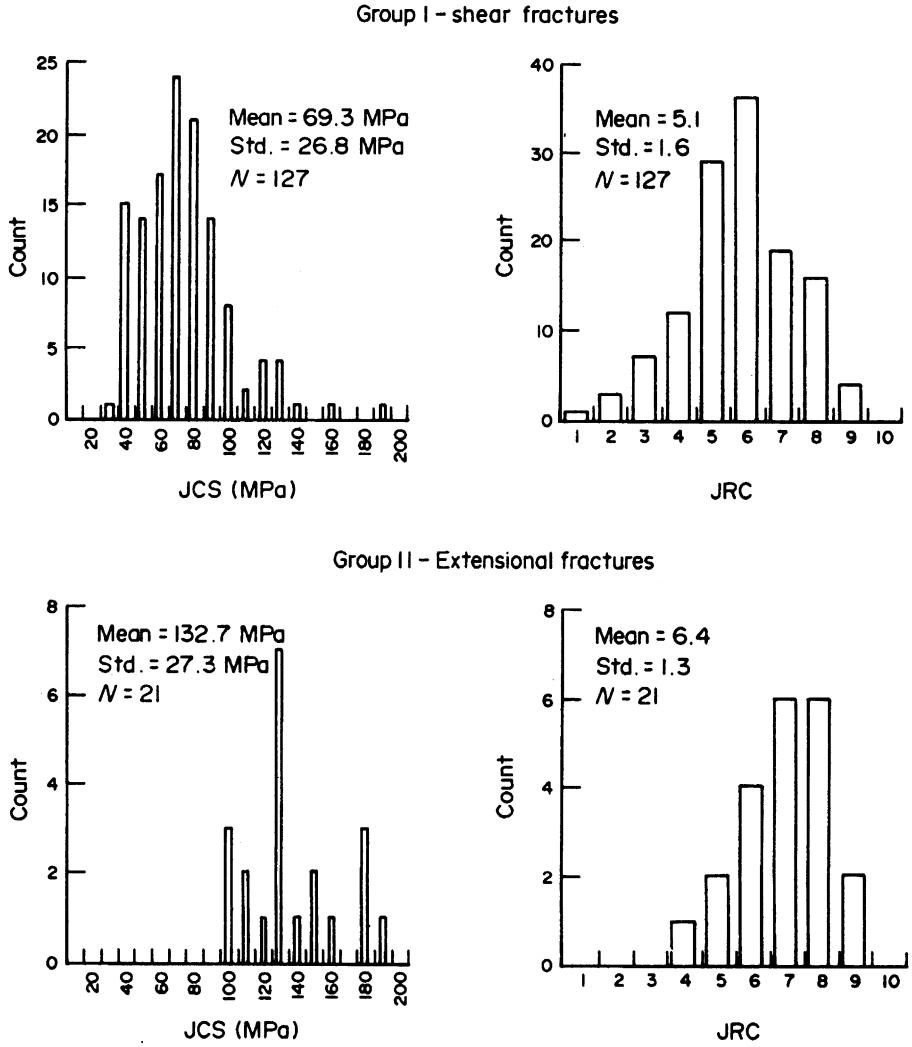

Fig. 13. Summary of JCS and JRC statistical data for Fracture Zone 2 shear joints (Group I) and Room 209 extensional joints (Group II) (after Ref. [44]).

in the domain between Fracture Zone 2.5 and 2 are intermediate in magnitude. Also, as can be seen in Figs. 10a–f, the direction of the maximum horizontal stress rotates by 90°, from the fault strike (Domains I and II) to the fault dip direction below Fracture Zone 2.

Overcoring and hydraulic fracturing measurements were successfully used to measure stresses above Fracture Zone 2, even if due consideration had to be given to the stress-relief induced anisotropy in interpreting the results at the 240 Level [54,56].

Below Fracture Zone 2, the high horizontal stresses induced subhorizontal fractures during hydraulic fracturing tests, that required particular inversion techniques in order to determine the stress tensor [57]. Incipient discing prevented the use of techniques that require a long intact core length to obtain a valid measurement (e.g. borehole-deformation gauges, CSIR and CSIRO gauges). A modified doorstopper technique was used [58]. Convergence measurements helped identify horizontal stress components only [59].

An under-excavation study using CSIRO HI cells around the bored vent raise from the 420 to the 240 Level [60, 61] provided an estimate of the complete tensor, but the results were affected by uncertainty in the CSIRO HI cell locations and orientations, small induced strains in the axial direction, and non-linear behavior around the boreholes when the advancing face was within 1 diameter of the instrument [62]. In the latter study, the estimates of both the magnitude and orientation of the maximum and intermediate stresses were well constrained, but those for the minimum principal stress (which is vertical) were not.

Results from an acoustic emission/microseismic (AE/MS) array installed in four inclined boreholes around the URL shaft [63] provided estimates for the maximum and minimum horizontal stress directions, which were

supported by observations of breakouts in the shaft, but provided no estimates for the stress magnitudes.

5.4. Two-dimensional model

A 2-D plane-strain model of the URL site is shown in Fig. 14. The plane in Fig. 14 is parallel to the dip direction of Fracture Zone 2, i.e. plane ABCD in Fig. 10a. The non-linear Finite Element program Phase2 [64] was used to carry out the following calculations.

Fracture Zones 2, 2.5 and 3 (see Fig. 10a) are modeled by means of non-linear joint elements: local joint slippage can occur if the shear stress on a joint element exceeds the shear strength as defined by the Coulomb parameters specified in Section 5.2.2. Normal and shear stiffness are constant, as described in Section 5.2.2.

The pink and grey granite rock masses are assumed to be linearly elastic (no yielding is allowed), with properties as specified in Section 5.2.3.

Gravity force is active, and a unit weight of $0.027\,\mathrm{MN/m^3}$ is assumed for the rock mass.

As shown in Fig. 14, zero horizontal displacements are prescribed at the left-hand side boundary of the model. Vertical displacements are prescribed to be zero at the bottom of the model. A constant horizontal displacement, X, must be defined at the right-hand boundary of the model. This is the boundary condition to be estimated, based on measured horizontal stresses parallel to the dip direction of Fracture Zone 2, and given in Table 3.

Fig. 15a shows the pattern of horizontal stresses in the dip direction, σ_{aa}, along the URL shaft for different values of the boundary displacement x. The lack of non-linearity is particularly evident at shallow depth, where the effect of slippage along the faults is more sensible. Fig. 15b confirms this conclusion: function $z_k(x)$ is plotted here for three depths, each representative of a stress domain defined in Fig. 10a.

Table 3
Measured horizontal in situ stresses parallel to the dip direction of Fracture Zone 2 (a-axis in Fig. 14) for the 2-D model. (After ref. [54])

k	Depth (m)	Stress (MPa):	Variance ($\mathrm{MPa^2}$)
		y_k	V_k
1	15.6	4.28	7.14
2	62.5	4.28	4.28
3	89.8	10.71	10.00
4	179.7	12.85	4.28
5	187.5	20.00	17.14
6	250.0	27.14	24.28
7	273.4	37.14	8.57
8	289.0	48.57	10.00
9	335.9	41.42	8.28
10	367.2	57.14	11.42
11	390.6	54.28	10.85
12	414.1	52.85	10.57
13	468.7	52.85	10.57

The data gathered by Herget [35] on the Canadian Shield will be used as a priori information. From Fig. 16, an average major principal stress of 20 MPa is obtained for the depth range applicable at the URL site. This is equivalent to a strain (assuming a Young's modulus of 60 GPa):

$$\varepsilon_1 = 20/60\times10^{-3} = 0.333\times10^{-3}. \quad (39)$$

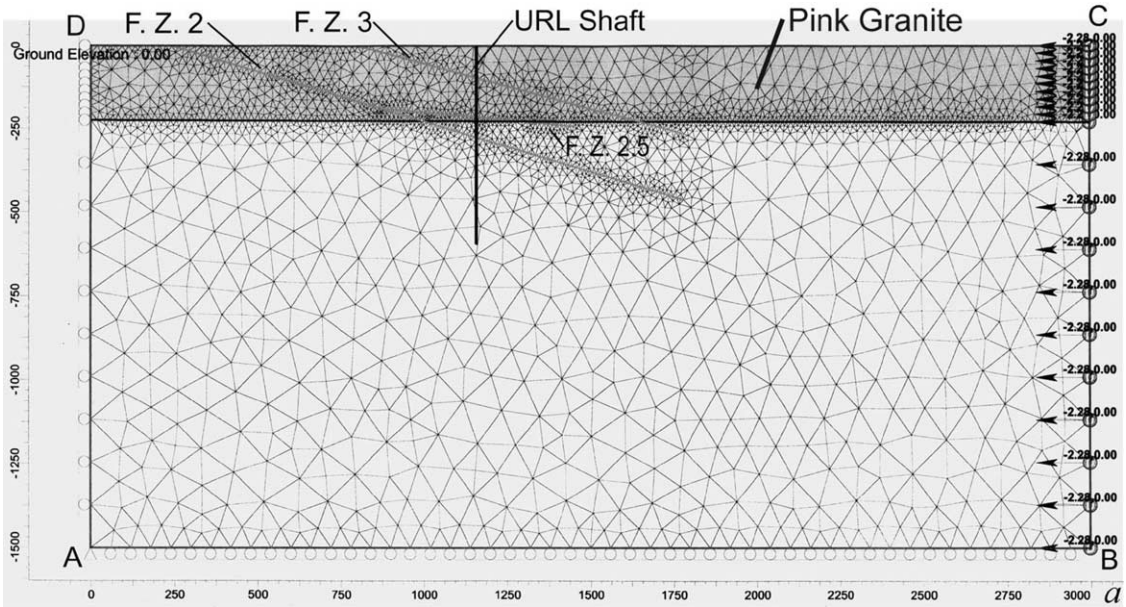

Fig. 14. Two-dimensional plane strain FEM model of the URL site; the vertical plane is parallel to the dip direction of Fracture Zone 2. Dimensions are in meters. Three-node triangular elements were used.

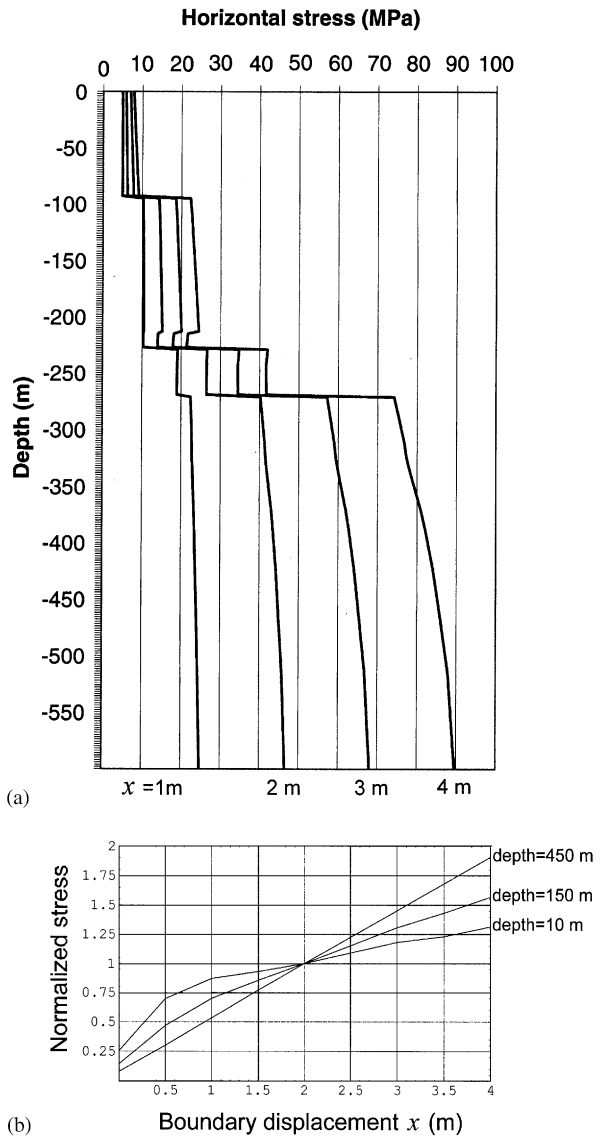

Fig. 15. (a) Stress profiles along the URL shaft due to four different boundary conditions; (b) Normalized stress $\sigma_{aa}(x)/\sigma_{aa}(x=2m)$ at three different depths; axis a is horizontal and parallel to the dip direction, as defined in Fig. 14.

The displacement necessary to yield this strain in a uniform strip of length $L = 3000$ m is:

$$\mu_X = (\varepsilon_1 \times L) = (1)\,\text{m}. \tag{40}$$

This is the a priori value of the boundary condition. A coefficient of variation of 45% is typical in stress measurements (see also Fig. 16), thus the covariance matrix is:

$$\mathbf{V}_{XX} = (0.2)\,\text{m}^2. \tag{41}$$

The a priori value of the displacement is also used as a starting point for the iterative procedure, i.e. $x^0 = \mu_x = 1$ m. The coefficients $h_k^j = z_k(x^{j-1})/x^{j-1}$ are given in Table 4. The results of the iterative procedure are given in Table 5, and portrayed in Figs. 17a–b. The procedure converges rapidly, and only 3 iterations are necessary to reach a relative error of 3.3%. Thus the FE model had to be run 3 times to reach a relative error of 3.3%. From a practical point of view, this error is more than satisfactory, especially when one considers the high degree of uncertainty involved in the stress measurements. The variance of the estimated boundary condition is 0.197, which is very close to the a priori value of 0.20. This is due to the large uncertainty associated with the updating stress measurements.

Fig. 18a presents the stress profiles in the dip-direction calculated at each iteration, together with the measured stresses. The match is satisfactory, and only in the depth range 100–200 m is the calculated horizontal stress slightly overestimated. The fast convergence rate of the iterative procedure is self-evident. Also, Figs. 17b and 18a show that iterations 4 and 5 do not improve on the match between measured and calculated stresses. This means that the limits of the FE model in representing the real rock mass behavior have been reached.

Plotted in Fig. 18b is the horizontal stress parallel to the fault strike. Because a 2-D plane-strain model was used, it is impossible to control the out-of-plane stresses, which turn out to be very different from the measured ones. This inconsistency motivated the preparation of the 3-D model described in Section 5.5.

The calculated horizontal stresses in the dip direction are plotted in Fig. 19. The lower stiffness of the pink granite induces lower stresses in the upper 200 m, even where faults are not present. The disturbance caused by the faults is well evident. However, the stress along the boundaries appears to be evenly distributed and fairly unaffected by this disturbance, i.e. there is no boundary effect on the calculated stresses along the URL shaft.

The yielded joint elements are represented in red color in Fig. 19. Fracture Zones 2 and 3 are completely yielded except in the very proximity of the tip, where stress concentrations develop. Fracture Zone 2.5 is in the elastic range. Figs. 20a–c show the shear displacements along Fracture Zone 2, the normal stresses across Fracture Zone 2, and the shear stresses on Fracture Zone 2, respectively. The same quantities are plotted in Figs. 21a–c for Fracture Zone 2.5, and in Figs. 22a–c for Fracture Zone 3.

The maximum calculated shear displacement occurs along Fracture Zone 2, and is less than 1 m. This figure is much less than the value observed in situ (>7 m) and highlights the difficulty in determining boundary conditions and the current in situ state of stress based on joint or fault displacements and geometry alone. Such methods were advocated, for example, by Angelier and co-workers [65,66].

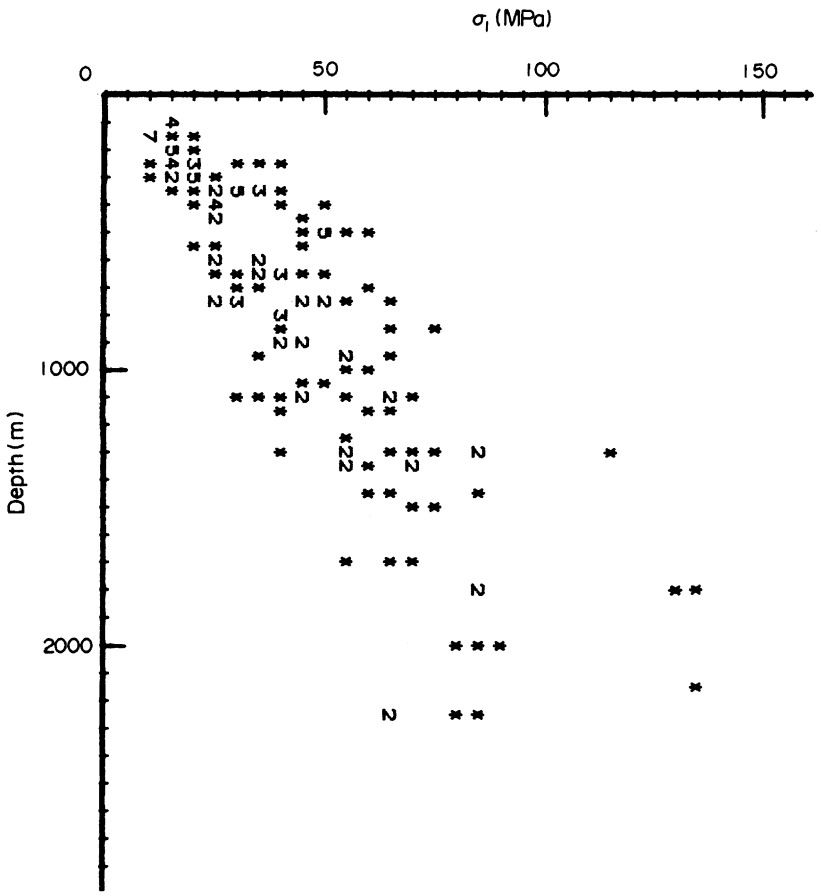

Fig. 16. Maximum principal stress with depth in the Canadian Shield. Numbers indicate the quantity of stress measurements that gave the same stress value (after Ref. [35]).

Table 4
Coefficients $h_k^j = z_k(x^{j-1})/x^{j-1}$ (MPa/m) used in the five iterations for the two-dimensional model of the URL site

k	$j=1$	$j=2$	$j=3$	$j=4$	$j=5$
1	4.58	2.645	2.46	2.43838	2.44161
2	4.8	2.935	2.75	2.74482	2.74846
3	4.89	3.09	2.92	2.91118	2.91065
4	10.55	7.6	7.27	7.26262	7.25908
5	10.59	7.65	7.32	7.30202	7.3073
6	19	13.25	12.64	12.6078	12.6157
7	22.46	19.9	19.49	19.5071	19.5154
8	22.54	20.15	19.78	19.8091	19.7915
9	22.94	21	20.62	20.6628	20.6726
10	22.27	21.5	21.2	21.2188	21.2162
11	23.47	21.85	21.47	21.4945	21.5011
12	23.68	22.05	21.73	21.7835	21.786
13	24.15	22.64	22.33	22.3876	22.3909

5.5. Three-dimensional model

5.5.1. Model preparation

AECL conducted an extensive survey aimed at determining the geometry of the faults and splays at the URL site [67]. The results are plotted in Figs. 23a–c. The structural discontinuities appear to be bowl-shaped and, except for a portion of Fracture Zone 3 (see Fig. 23a), they cannot be treated as planar features. Also indicated in Fig. 23c are the limits of the 3-D Finite Element model of the site, and the position of the URL shaft.

Figs. 23a–c were obtained by interpolating the spatial coordinates of the discontinuities; to this end, a Kriging technique was used within the program Surfer, Version 6.4 [68]. Because the fault depth data were not taken at a regular horizontal grid, the later program was also used to obtain the depth of Fracture Zones 2 and 3 at a regular horizontal grid (49×51 m spacing along x_1 and x_2, respectively). Then, these spatial coordinates were imported into the Finite Element program Strand7, Version 1.03 [23], and the mesh was prepared. The splay Fracture Zone 2.5 was not modeled because few data were available on its geometry (see Fig. 23c). Also, the 2-D analysis (Section 5.4) showed that Fracture Zone 2.5 did not yield, and, consequently, its importance was deemed secondary in a first assessment of the problem in hand.

Table 5
Results of the iterative procedure for the 2-D model of the URL site

	$j=0$	$j=1$	$j=2$	$j=3$	$j=4$	$j=5$
x^j (m)	1	1.99	2.2548	2.2843	2.2813	2.2810
Relative error R^j (%)	54.3	14.7	4.7	3.2	3.3	3.3

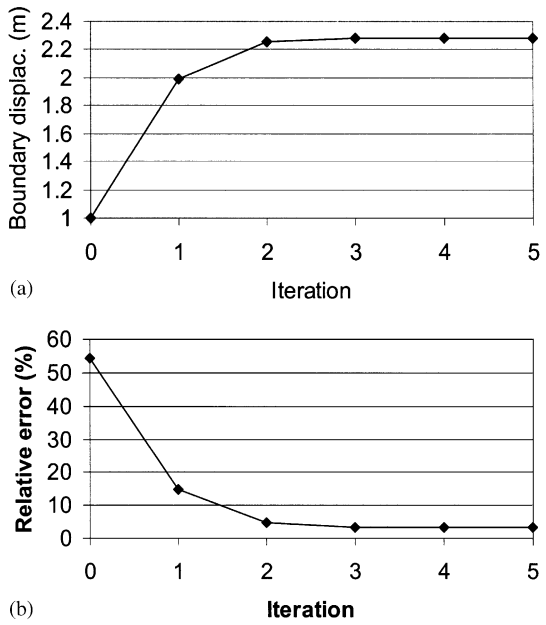

Fig. 17. (a) Computed boundary stresses at each iteration (iteration = 0 refers to the starting state of stress); (b) square mean root of the difference calculated-measured displacements at each iteration.

Three blocks were modeled (see Fig. 24): Block 1 extends between the surface and Fracture Zone 3, Block 2 between Fracture Zone 3 and Fracture Zone 2, and Block 3 between Fracture Zone 2 and the bottom of the model at a depth of 1500 m.

Zero gap, point contact beam elements were used at the fault interfaces in order to connect nodes on both sides of the 0.01 m-high gap between the blocks. This type of element provides stiffness only in compression, and only when the distance between the nodes to which it is connected becomes zero. Friction coefficients are assigned in the principal axis directions of the beam; they control the amount of lateral force that can be transferred. In each direction, the lateral force cannot exceed the axial force times the respective coefficient. Because an isotropic friction angle of 20° was assumed for the faults (see Section 5.2.2), the friction coefficients are equal in the principal axis directions of the beam, and take on the value $\tan(20^\circ) = 0.364$. The axial stiffness of the beam was set equal to 10^8 MN/m. The following options were set:

(a) Dynamic stiffness: if set, this option allows the solver to increase and/or decrease the stiffness dynamically, to better enforce the contact conditions. In subsequent iterations, the solver adjusts the stiffness to a more suitable value, depending on the state of the gap. If the stiffness is too small, there will be some penetration of material. In this case, the solver increases the stiffness to better enforce the contact requirement.
(b) Use in first iteration: this is used as an aid to the solver. If it is known that initially the elements are in contact, by setting this option the solver assembles the elements in the first iteration.
(c) Update direction: this is only relevant to geometric nonlinear analysis. If this option is set, the position and hence direction of the contact element is updated as the structure deforms.

Eight-node brick elements (Brick8) were initially used for the three blocks. However, condensation failure occurred due to excessive distortion of some elements. The Brick8 element in Strand7 includes additional internal "bubble" functions to enhance its behavior and alleviate so-called "locking" problems, i.e. to make the element more flexible. The condensation procedure involves the inversion of a sub-matrix. If the sub-matrix cannot be inverted, the condensation fails. The problem was solved by transforming the Brick8 elements into 4-node tetrahedral elements, which did not collapse for excessive distortion.

The 3-D model features 28,734 tetrahedral elements, 1,962 point contact beams, 8,124 nodes, and 22,949 degrees of freedom.

The three blocks are assumed to be linearly elastic. Blocks 1 and 2, which model the pink granite, are transversely isotropic with the elastic properties as given in Section 5.2.3. The plane of transverse isotropy is vertical, and, as indicated in Fig. 23c, its dip direction is equal to 125°. Block 3 is assumed to be isotropic with the properties of the grey granite as given in Section 5.2.3. The gravity force is active, and a unit weight of 0.027 MN/m^3 is assumed for the rock mass.

The analysis is non-linear because the element geometry and the contact element status are updated at each iteration. The non-linear static solver performs the following steps:

(1) Initializes the nodal displacement vector **u**.
(2) Sets the current load increment.

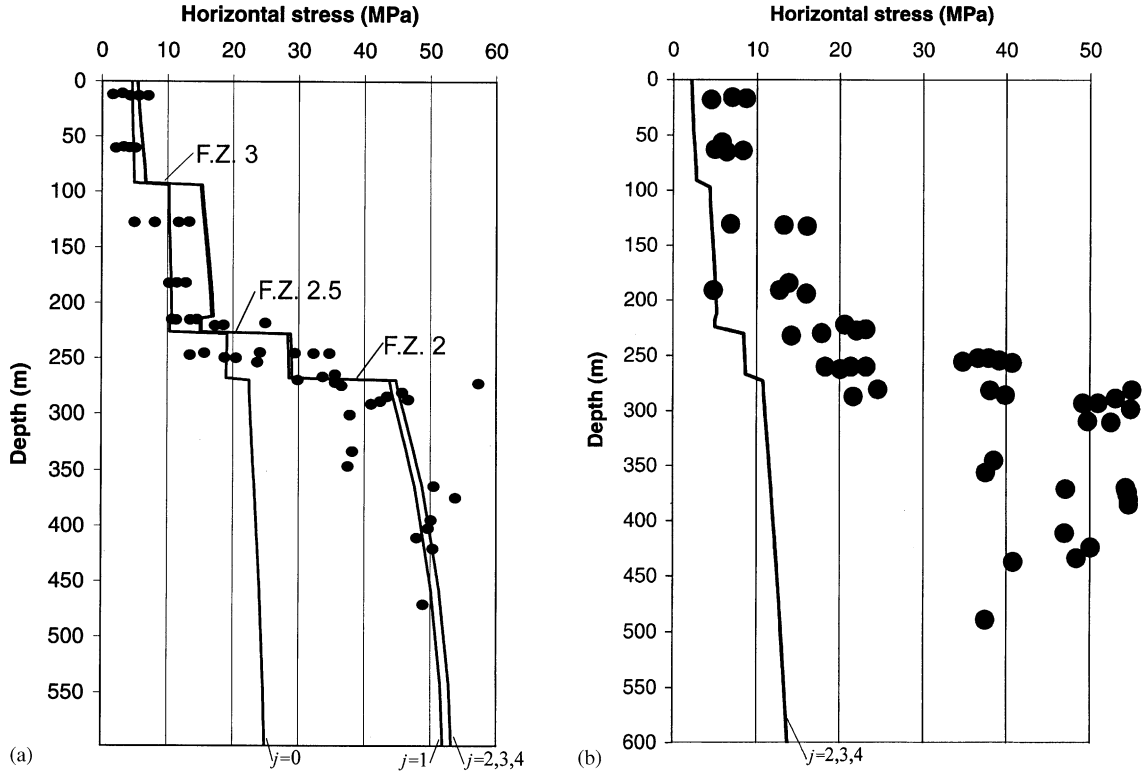

Fig. 18. Computed (continuous lines) and measured (dots) horizontal stresses along the URL shaft. (a) Stresses parallel to the dip direction of the faults at the URL shaft ($j = 0$ refers to the a priori information); (b) Stresses parallel to the strike direction of the faults at the URL shaft (only the final computed stresses are shown).

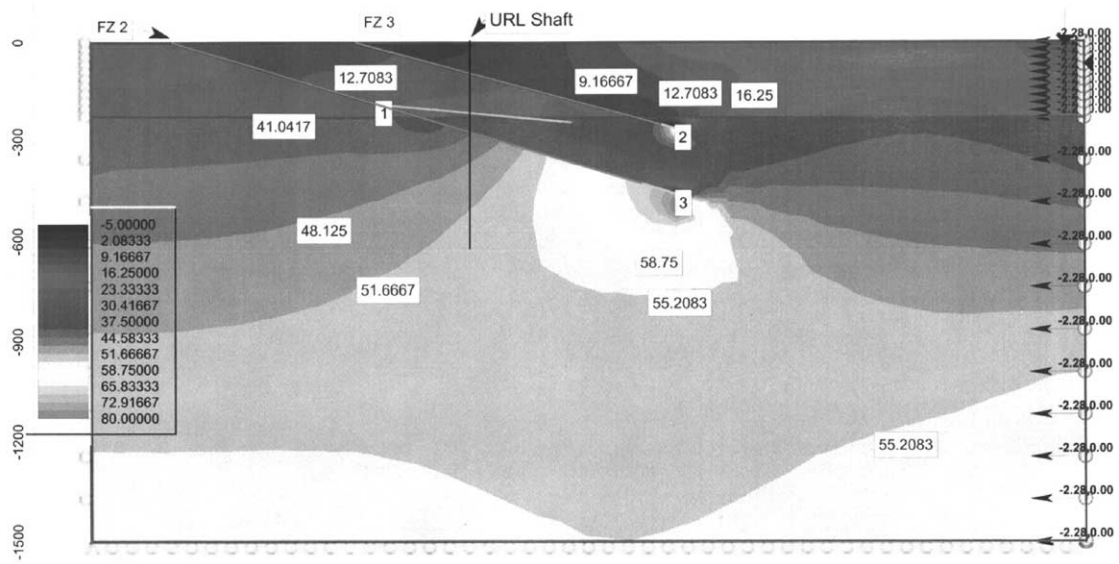

Fig. 19. Contours of calculated horizontal stresses in the dip direction for the estimated boundary condition.

(3) Calculates and assembles the element stiffness matrices using the current geometry, equivalent element force vectors, and external nodal force vectors. Constraints are also assembled in this process, and the constant terms in the enforced displacements are combined and applied. At the end of this assembly procedure, the following linear equation system of equilibrium is formed:

$$\mathbf{K}(\mathbf{u})\,\Delta\mathbf{u} = \mathbf{R}, \tag{42}$$

where $\mathbf{K}(\mathbf{u})$ is the current global stiffness matrix, $\Delta\mathbf{u}$ is the displacement increment vector, and $\mathbf{R}$ is

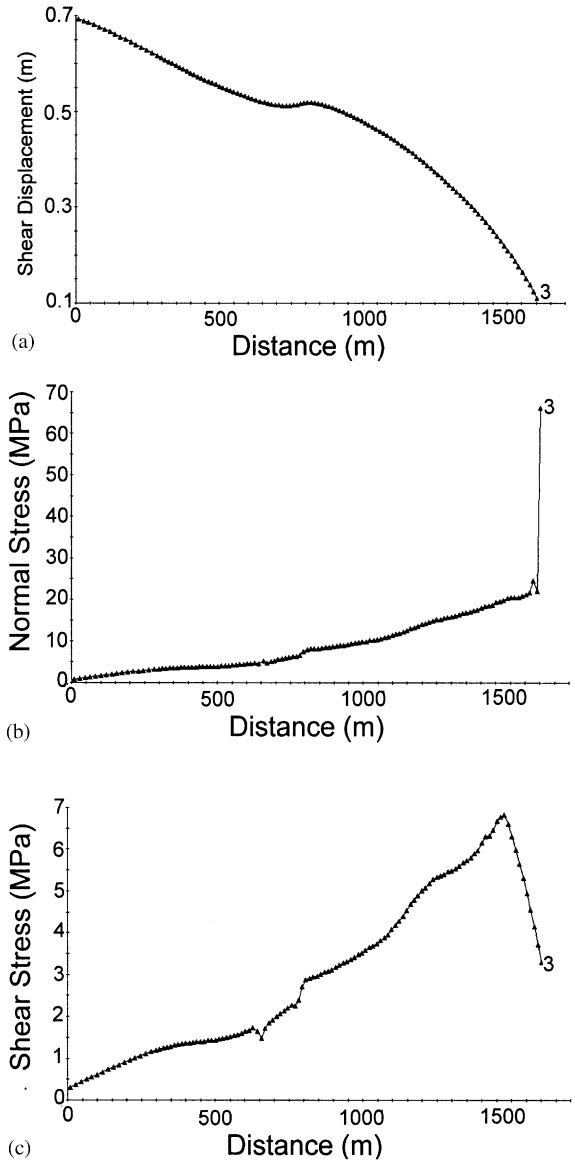

Fig. 20. Calculated quantities along Fracture Zone 2 for the estimated boundary condition (the location of the number on the graph corresponds to the location of the same number in Fig. 19, i.e. the fault tip). (a) Shear displacements; (b) normal stress across the fault; (c) shear stress.

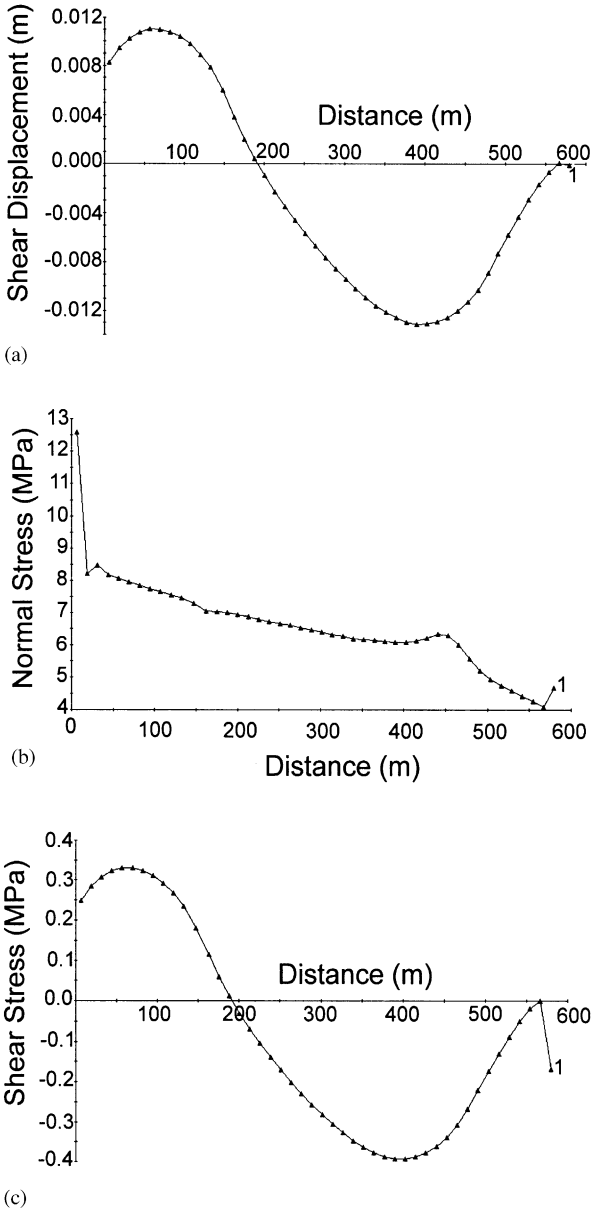

Fig. 21. Calculated quantities along Fracture Zone 2.5 for the estimated boundary condition (the location of the number on the graph corresponds to the location of the same number in Fig. 19). (a) Shear displacements; (b) normal stress across the fault; (c) shear stress.

the global residual force vector or unbalanced force vector with:

$$\mathbf{R} = \mathbf{P} - \mathbf{F}(\mathbf{u}), \tag{43}$$

in which $\mathbf{P}$ and $\mathbf{F}(\mathbf{u})$ are the current external force and element nodal force vectors, respectively.

(4) Solves Eq. (42) for $\Delta\mathbf{u}$.
(5) Updates the total nodal displacement vector $\mathbf{u}$.
(6) Checks convergence. If the convergence criteria are satisfied, go back to Step 2 to start the next load step or stop at the last load step. Otherwise, continue the iteration and go back to step 3.

In each of the following analyses, two load increments were applied:

(a) Only the gravity force acts on the model, and all boundary conditions are set to zero (consolidation phase).
(b) The boundary conditions are applied.

The computational time taken for each analysis was about 10 h on a PC Pentium II 266 Mhz with 128 MB RAM.

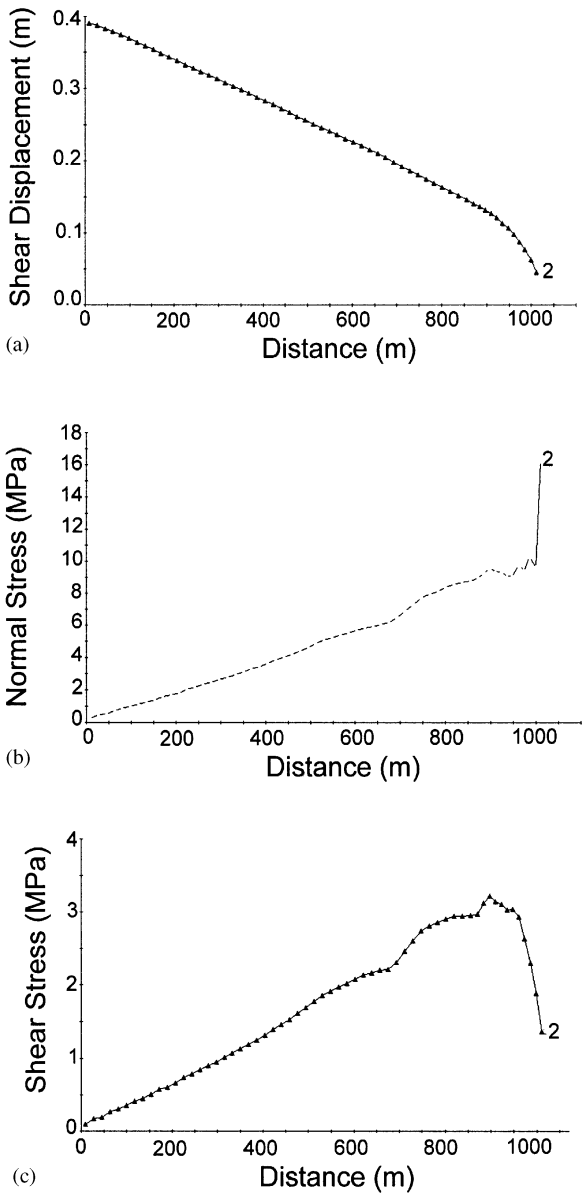

Fig. 22. Calculated quantities along Fracture Zone 3 for the estimated boundary condition (the location of the number on the graph corresponds to the location of the same number in Fig. 19, i.e. the fault tip). (a) Shear displacements; (b) normal stress across the fault; (c) shear stress.

5.5.2. Boundary condition estimation

With reference to Fig. 24, only Block 3 is subject to constraints acting during both load increments *a* and *b* described in Section 5.5.1. More specifically, points on face ADGH of Block 3 are constrained against displacements along the x_1-axis, points on face EFGH of Block 3 are constrained against displacements along the x_2-axis, and points on face ABEH of Block 3 are constrained against displacements along the x_3-axis. The boundary conditions to be estimated are the uniform horizontal displacements applied to faces ABCD (X_1) and BEFC (X_2) of Blocks 1, 2, and 3. When non-zero boundary conditions X_1 and X_2 are applied, the constraints applied to Block 3 allow Blocks 1 and 2 to slide past each other, and to Block 2 to slide past Block 3.

The input (observable) data are the horizontal stresses along the URL shaft. It is to be noted that the vertical faces of the model (see Figs. 23c and 24) are not parallel to the principal stress directions determined in situ. In fact, the later are parallel and orthogonal to the plane of transversely isotropy of the pink granite, which strikes N35° E (see Fig. 23c), whereas the vertical faces of the FE model strike North–South or East–West.

As in the 2-D model, Herget's data [35] on the stress state in the Canadian Shield were used here as a priori information (see Fig. 16). The length of the FE model in the x_1-direction is 1275 m, and the length in the x_2-direction is 1690 m. In order to estimate the a priori boundary conditions, it is assumed that the model has no joints and is isotropic and homogeneous, with a Young's modulus equal to 60 GPa. If the Poisson's effect is disregarded, the displacement necessary to produce a horizontal stress σ_{11} equal to 20 MPa is:

$$\delta_1 = \frac{20}{60000}1275 = 0.425\,\text{m}.$$

Similarly, the displacement necessary to induce a horizontal stress σ_{22} equal to 20 MPa is:

$$\delta_2 = \frac{20}{60000}1690 = 0.563\,\text{m}.$$

Thus, the a priori mean is $\mu_X = (0.425, 0.563)^{\mathrm{T}}$ m. A coefficient of variation of 45% is assumed (see also Fig. 16), and the covariance matrix is:

$$\mathbf{V}_{XX} = \begin{pmatrix} 0.085 & 0 \\ 0 & 0.1126 \end{pmatrix} \text{m}^2.$$

The observed horizontal stresses in the x_1 and x_2 directions are given in Tables 6a and 6b, together with the observed uncertainty. The observed quantities are supposed to be independent, thus only the non-zero diagonal entries of matrix **V** are given in Table 6.

The a priori mean boundary displacements are also used as a starting point in the iterative estimation procedure.

The estimated boundary conditions and the relative error at each iteration are given in Table 7, and are plotted in Figs. 25a–b, respectively. These figures show that the a priori information is a good starting point because the final estimated boundary conditions for X_1 and X_2 are 67% and 20% larger than the a priori mean values, respectively. The relative error eventually stabilizes at 24.4%, which is a much higher value than that obtained in the 2-D model (3%). This result is due to the complex 3-D geometry of the faults. Also, in the 2-D model, no attempt was made to reproduce the

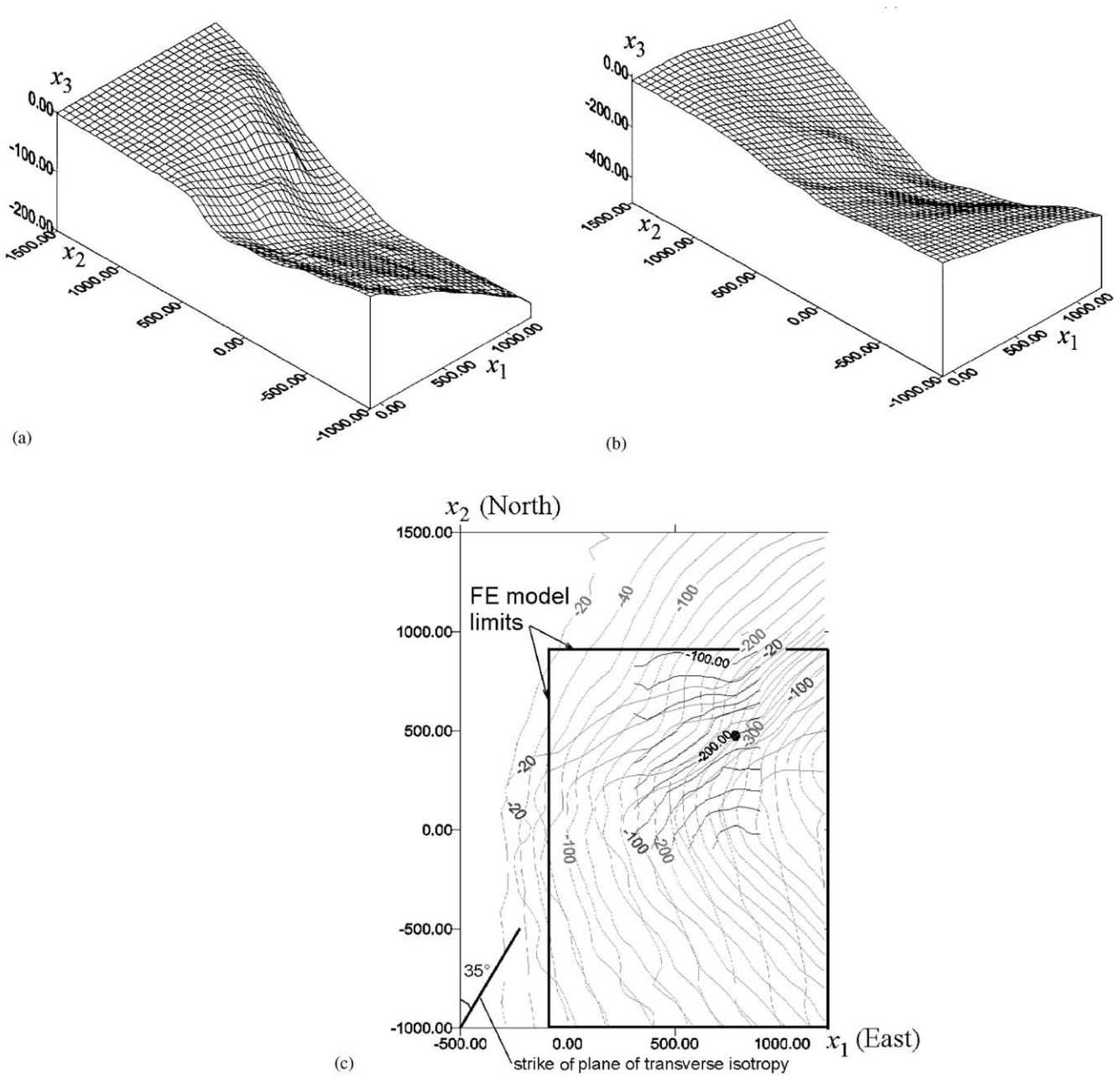

Fig. 23. Fault geometry at the URL site. (a) Axonometric view of Fracture Zone 3; (b) axonometric view of Fracture Zone 2; (c) contour lines (interval = 20 m) of Fracture Zone 3 (blue), Fracture Zone 2.5 (black), Fracture Zone 2 (red): a dot marks the position of the URL shaft. In Fig. 23c, the strike of the plane of transverse isotropy for the pink granite is also indicated. Axis x_1 and x_2 are horizontal, and positive toward the East and the North, respectively; x_3 is vertical and positive upwards. Lengths are in meters. The vertical coordinates have been translated so that the zero reading is at the URL shaft collar (289.9 m a.s.l.). Thus, the coordinates of the URL shaft collar are (784.959, 475.031, 0).

out-of-plane measured stresses, and so less data points were considered. Because the relative error R^j is always less than 100% (see Table 7), the "augmented secant method" (Section 4.2) was used throughout. The iterative procedure proposed shows fast convergence in spite of the complexity of the problem in hand. Only three iterations (i.e. 9 model runs for a total of about 90 h of computational time) were necessary to arrive at a satisfactory estimate of the boundary conditions.

This good agreement is confirmed by Figs. 26a–b, which show the calculated and the measured horizontal stresses along the URL shaft. For $j = 3$, the calculated stresses reproduce reasonably well the measured values, which appear to be very scattered, especially in the strike direction.

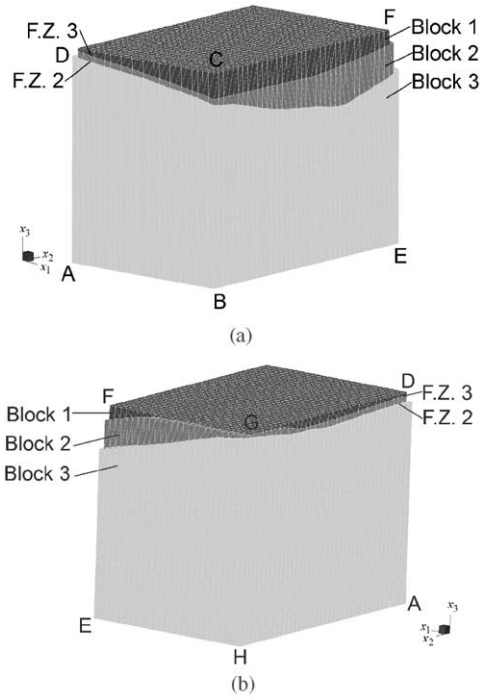

Fig. 24. (a,b) Three-dimensional views of the Finite Element model of the URL site.

Table 6

K	Depth (m)	y_k (MPa)	$V(k,k)$ (MPa^2)
(a) Measured horizontal in situ stresses parallel to the x_1-direction for the 3-D model of the URL site			
1	15.6	4.28	7.14
2	62.5	4.28	4.28
3	89.8	10.71	10.00
4	179.7	12.86	4.28
5	187.5	20.00	17.14
6	250.0	27.14	24.28
7	273.4	37.14	8.57
8	289.1	48.57	10.00
9	335.9	41.43	8.28
10	367.2	57.14	11.43
11	390.6	54.28	10.86
12	414.1	52.86	10.57
13	468.7	52.86	10.57
(b) Measured horizontal in situ stresses parallel to the x_2-direction for the 3-D model of the URL site			
14	15.6	7.14	5.71
15	62.5	6.43	4.28
16	89.8	10.71	10.00
17	179.7	10.71	11.43
18	187.5	18.57	10.00
19	250.0	22.86	22.86
20	273.4	31.43	20.00
21	289.1	48.57	5.71
22	335.9	31.43	6.28
23	367.2	47.14	9.43
24	390.6	42.86	10.00
25	414.1	45.71	10.00
26	468.7	38.57	7.71

Table 7
Estimated boundary conditions and relative error for the 3-D model of the URL site

Iteration (j)	(x_1^j, x_2^j) (m)	$R^j = \sqrt{\sum_k^{2b} (\xi_k^{j+1} - y_k)^2 / \sum_k^{2b} (y_k)^2}$ (%)
0	(0.425, 0.563)	30.0
1	(0.672, 0.534)	21.4
2	(0.618, 0.670)	24.5
3	(0.710, 0.670)	24.4

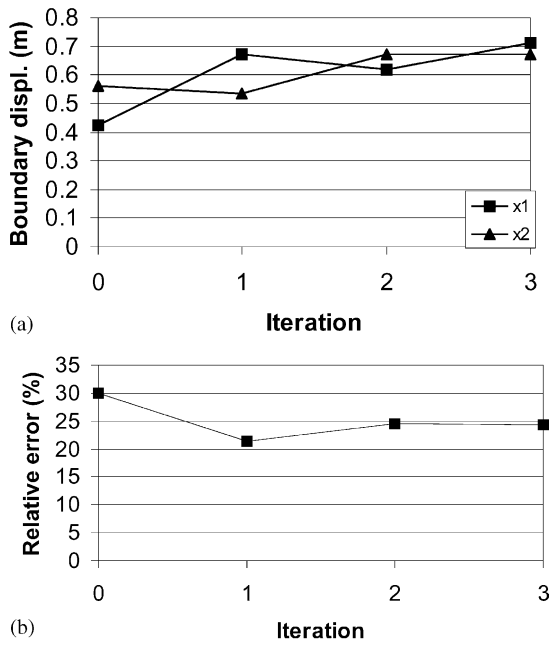

Fig. 25. (a) Computed boundary displacements at each iteration (iteration = 0 refers to the starting state of stress); (b) square mean root of the difference calculated-measured displacements at each iteration.

It is interesting to compare Figs. 26a–b, relative to the 3-D model, with Figs. 18a–b, relative to the 2-D model. The calculated horizontal stresses parallel to the fault dip (Figs. 18a and 26a) are very similar, except for the absence of the stress discontinuity across Fracture Zone 2.5, which was not considered in the 3-D model. The computed stresses parallel to the fault strike are instead completely different (compare Figs. 18b and 26b). Specifically, the 3-D model was able to reproduce the measured pattern very well, with a slight over-estimation between 100 and 250 m depth, whereas the 2-D model completely failed to give a reasonable picture of the out-of-plane stress.

Consider two 10°-aperture cones having the dip and the strike direction of the faults as their respective axes. In the 3-D FE model, for $j = 3$, the major and intermediate principal stresses are found to be always within these two cones. As a consequence, the horizontal

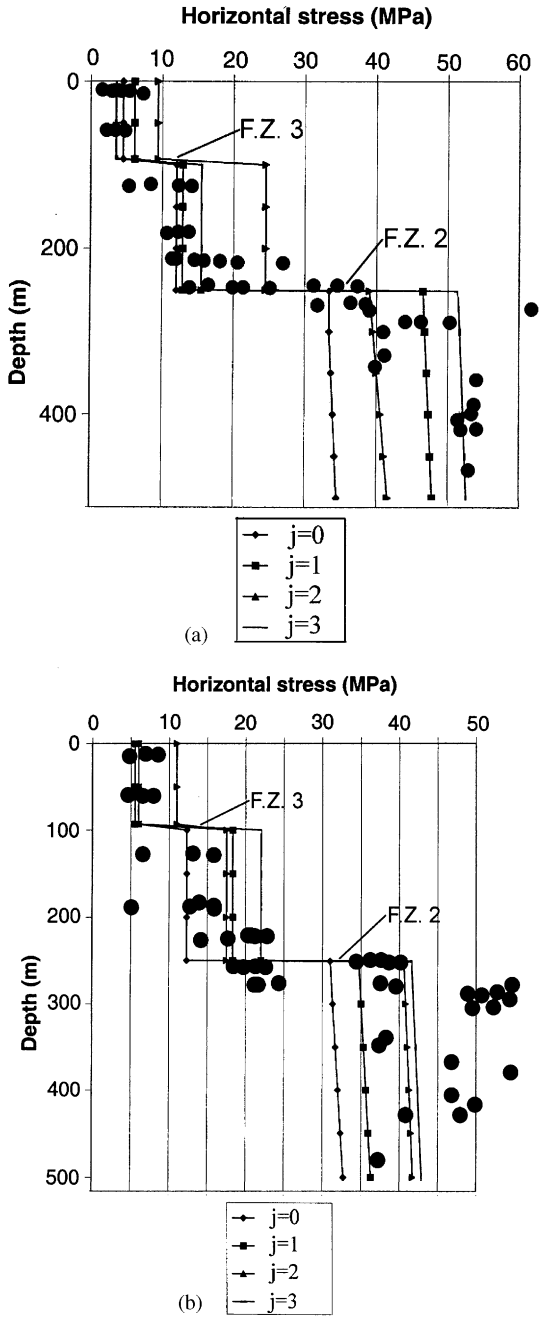

Fig. 26. Computed and measured horizontal stresses along the URL shaft. (a) Stresses parallel to the dip direction of the faults at the URL shaft ($j = 0$ refers to the a priori information); (b) Stresses parallel to the strike direction of the faults at the URL shaft, see Fig. 23c ($j = 0$ refers to the a priori information).

stresses plotted in Figs. 26a–b are a very good approximation to the major and intermediate principal stresses. These horizontal stresses, for $j = 3$, display the 90° rotation across Fracture Zone 2 (depth 250 m) that was observed in situ (see Figs. 10a–f).

Contours of the horizontal stresses parallel to the dip and the strike direction of the faults are plotted in Figs. 27a–b, respectively. They show the presence of stress discontinuities across the faults and the comparatively low stress acting in Blocks 1 and 2 (the shear resistance along the faults is overcome throughout, i.e. the discontinuities are completely yielded). This phenomenon is due to slippage along the faults, which is confirmed in Figs. 28a–b. These later figures portray the displacement components parallel to the dip and to the strike directions of the faults, respectively. The relative shear displacement across the faults is never greater than 1 m, whereas the displacement measured in situ at the URL shaft intersection is greater than 7 m. This result confirms the difficulty in using measured fault displacements to estimate the current state of stress or boundary conditions for a rock mass model, as already observed in the 2-D model.

This is because fault relative displacements have been accumulating over the geologic history of the rock mass, since the fault formation. In addition, such displacements are the results of the Earth crust evolution, which is impossible to track, let alone finding an appropriate constitutive model for the intact rock, discontinuities and rock mass over geologic eras, and determining initial and boundary conditions with the precision and resolution needed for engineering projects. This conclusion is in keeping with Cornet's [69] about in situ stresses: "Because the exact geological history of rock masses will never be known precisely, because the constitutive equations describing the mechanical behavior of rocks remain fairly approximate, and because the detailed structure of a rock mass cannot be determined exactly, it is impossible to evaluate the natural stress field by straight computation".

From an engineering point of view, it seems more reasonable and meaningful to look at the current state of affairs, by measuring the current rock mass response to disturbances, and to estimate the boundary conditions that allow the rock mass model $\mathfrak{M}$ to reproduce those disturbances at best. Such model $\mathfrak{M}$ with the estimated boundary conditions can then be used to "go forward" and predict the response of the rock mass under study to future engineered disturbance (tunnels, caverns, excavations, dams, etc.).

6. Conclusions

Bayesian procedures have been proposed to determine the boundary conditions for a rock mass model. These procedures make it possible to incorporate a priori information and to update the boundary conditions as soon as new information becomes available. Simple synthetic examples have shown the relative importance of a priori and updating information.

The procedures proposed in this paper are quite general because mixed basic data (displacement components, stresses, and strains) and mixed boundary

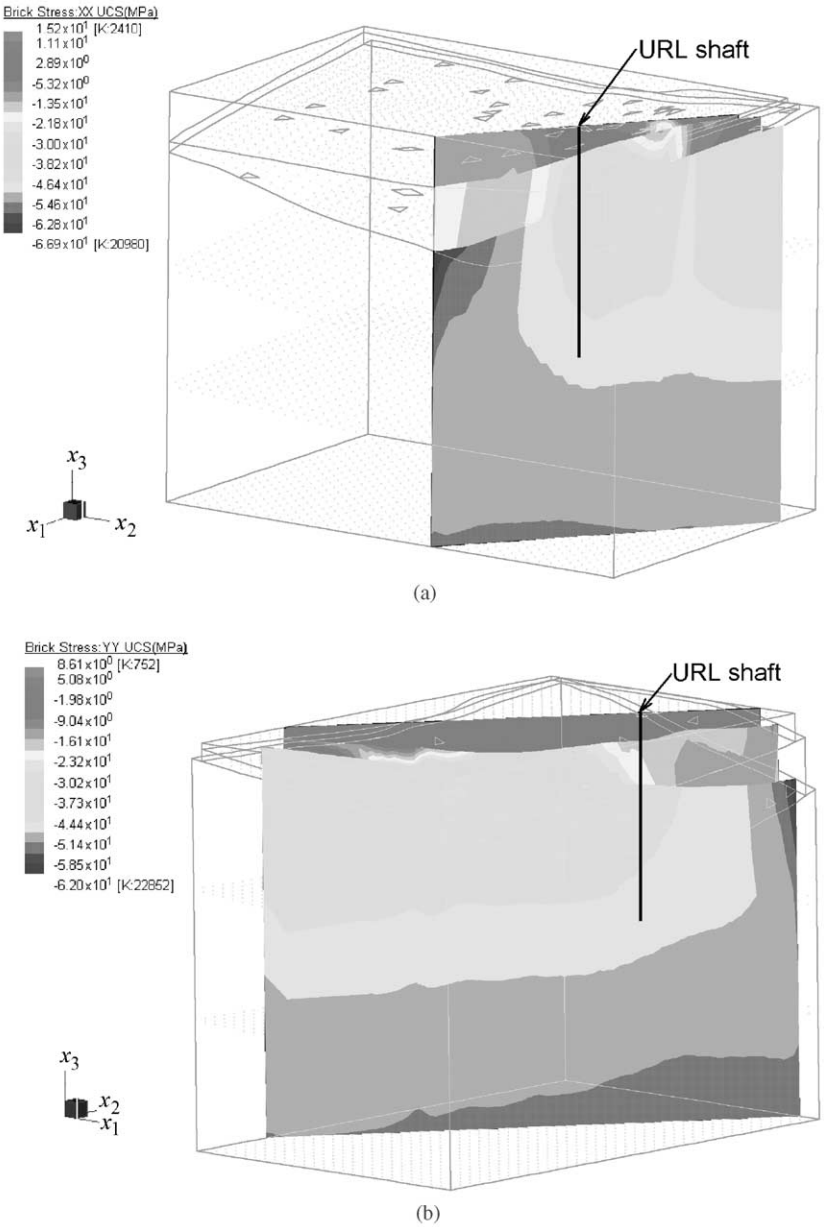

Fig. 27. Contours of horizontal stresses: (a) parallel to the dip direction of the faults; (b) parallel to the strike direction of the faults. The spatial attitude of the faults is determined at the intersection with the URL shaft, see Fig. 23c. Compressive stresses are negative.

conditions (stresses, displacement components) may be used without difficulty. Also, any rock mass model can be used, thus engineers can continue utilizing their own software used for analyzing the rock mass.

When the rock mass can be modeled as linearly elastic, the boundary conditions are computed in a one-step solution. When the rock mass has a non-linear behavior, an iterative procedure must be followed.

The 2-D and 3-D applications to the URL site have shown the fast convergence rate of the iterative procedure, despite the high degree of non-linearity involved in the models, and the complex geology of the site.

The 2-D model of the URL was able to reproduce the observed stress pattern in the dip direction of the faults, but not the stress pattern in the strike direction of the faults.

The 3-D model of the URL was able to reproduce the observed stress pattern both in the dip and in the strike direction of the faults.

Discontinuity geometry and slickenside direction and magnitude alone are not always sufficient in order to infer the present in situ state of stress in a rock mass and the correct boundary conditions for the model under consideration. Measurements of the current response of the rock mass (in terms of displacement components,

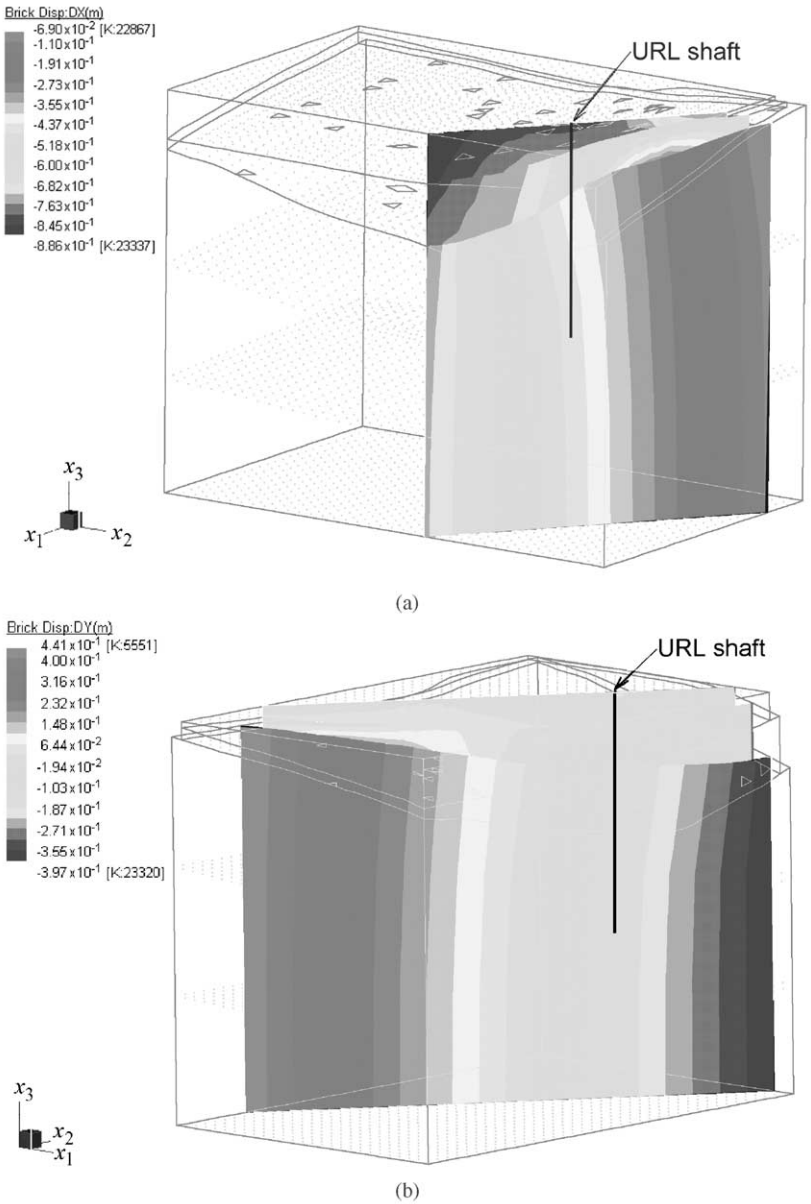

Fig. 28. Contours of horizontal displacement components: (a) parallel to the dip direction of the faults; (b) parallel to the strike direction of the faults. The spatial attitude of the faults is determined at the intersection with the URL shaft, see Fig. 23c.

stresses, strains) to disturbances (e.g. excavation) must be conducted in order to pin down the current boundary conditions of a rock mass model.

Instrumental to a good fit between measured and computed values is a thorough understanding of the site geology. In particular, the faults' geometry and structural origin played a decisive role in building the model.

Acknowledgements

This research is funded by National Science Foundation under Grant No. CMS-9713559. The authors wish to thank Dr. N.A. Chandler (AECL, Canada) for providing them with extensive data and material on the Underground Research Laboratory (URL) of Atomic Energy Canada Limited (AECL), Canada. The comments of the unknown Reviewers and of the Editor are greatly appreciated.

Appendix A

The classical statistical approach to assessing distribution parameters assumes that the parameters are constant (but unknown), and random sample statistics are used as estimators (i.e. as approximations to these parameters). This approach entails point estimates

and confidence intervals [32], and its major disadvantage is that it provides no way for combining different sources of information, for example judgmental and observational.

In contrast, the Bayesian approach assumes that the distribution parameters are random variables with known probability distributions. Uncertainty associated with the estimation of the parameters can be formally combined (through Bayes' theorem) with the inherent variability of the basic random variable. Using this approach, subjective judgments based on intuition, experience or indirect information are incorporated systematically with observed data to obtain a balanced estimation. The requirement that one must model the population of each parameter by defining the form of its density function with known moments is the major disadvantage of this technique [33]. This requirement makes Bayesian methods parametric in nature.

The definitions given in this appendix are taken from Lewis and Odell [33].

Definition 1. Let the domain of a real function g be an n-dimensional space of real numbers. The expected value of g as a function of the random variables $X_1,\ldots,X_n$ is defined as:

$$\mu_G = E[g(X_1,\ldots,X_n)] := \int_{x_1}\ldots\int_{x_n} g(x_1,\ldots,x_n)\, f_{X_1,\ldots,X_n}(x_1,\ldots,x_n)\,\mathrm{d}x_1\ldots\mathrm{d}x_n, \tag{A.1}$$

where $f_{X_1,\ldots,X_n}(x_1,\ldots,x_n)$ is the joint probability density function of the random variables $X_1,\ldots,X_n$.

Definition 2. The expected value (or mean vector) of an $n\times 1$ random vector $X=(X_1,\ldots,X_n)^{\mathrm{T}}$ is:

$$\mathbf{E}[X] := (E[X_1],\ldots,E[X_n])^{\mathrm{T}}. \tag{A.2}$$

Definition 3. The covariance matrix of a random vector $X=(X_1,\ldots,X_n)^{\mathrm{T}}$, whenever it exists, is the symmetric positive definite matrix:

$$\mathbf{E}[(X-\mathbf{E}[X])\,(X-\mathbf{E}[X])^{\mathrm{T}}]. \tag{A.3}$$

The ith diagonal element in Eq. (A.3) is the variance of X_i, and the (i,j)th entry is the covariance of X_i and X_j.

Following Lewis and Odell [33], let θ be a parameter (a state vector unknown to the observer) that one wishes to *estimate* using observations and data usually distorted by *random error e,* sometimes called *noise*. To illustrate, let Y be a random variable such that $Y=\theta+e$, where θ is an unknown parameter, and e is a random variable with zero mean and known variance. Suppose that a random sample $y_1,\ldots,y_n$ of size n is going to be observed (i.e. in this experiment the successive samples are independent and the underlying population (or the distribution of Y) remains the same from one sample value to another). Each sample value can be thought of as being a random variable Y_i, and thus the sample mean is now a random variable itself and is written as:

$$\bar{Y} := \frac{1}{n}\sum_{i=1}^{n} Y_i. \tag{A.4}$$

The sample mean $\bar{Y}$ is called an estimator of the parameter θ.

Definition 4. An estimator $\hat{\Theta}$, sometimes called a statistic, is a function of the observation vector $Y=(Y_1,\ldots,Y_n)^{\mathrm{T}}$, which does not depend on the parameter θ, and estimates θ.

Definition 5. An estimator $\hat{\Theta}$, is said to be unbiased if and only if:

$$E[\hat{\Theta}] = \theta. \tag{A.5}$$

Let the probability density function of the observations $Y=(Y_1,\ldots,Y_n)^{\mathrm{T}}$ and of the parameter Θ be:

$$f(y,\theta) = h_{Y|\Theta}(y|\theta)g_{\Theta}(\theta) = h_{\Theta|Y}(\theta|y)g_Y(y), \tag{A.6}$$

where $h_{Y|\Theta}$ and $h_{\Theta|Y}$ denote the conditional density function of Y given Θ, and Θ given Y, respectively, while g_{Θ} and g_Y are the marginal density functions of Θ and Y, respectively.

Definition 6. A loss function $l(\hat{\Theta},\theta)$ is a nonnegative function such that:

(1) $l(\hat{\Theta},\theta)\geqslant 0$ for all admissible values of Θ and $\hat{\Theta}$.
(2) For each admissible value of Θ there is at least one $\hat{\Theta}$ such that $l(\hat{\Theta},\theta)=0$.

Definition 7. Let Θ be distributed according to $g_{\Theta}(\theta)$, and Y according to $h_{Y|\Theta}(y|\theta)$; then the Bayes estimator for Θ, say $\hat{\Theta}$, is the statistic $\hat{\Theta}=\hat{\Theta}(Y_1,\ldots,Y_n)$ such that the expected value of the loss function is minimized; that is, minimize:

$$E[l(\hat{\Theta},\theta)] = \int_{\theta}\left(\int_{y_1}\ldots\int_{y_n} l(\hat{\Theta},\theta)h_{Y|\Theta}(y|\theta)\,\mathrm{d}y_1\ldots\mathrm{d}y_n\right)\times g_{\Theta}(\theta)\,\mathrm{d}\theta. \tag{A.7}$$

From Eq. (A.6), one obtains Bayes theorem by isolating $h_{Y|\Theta}$:

$$h_{Y|\Theta}(y|\theta) = \frac{h_{\Theta|Y}(\theta|y)g_Y(y)}{g_{\Theta}(\theta)} \tag{A.8}$$

Upon substitution of Eq. (A.8) into Eq (A.7), the expected value of the loss function takes on

the expression:

$$E[l(\hat{\Theta},\theta)] = \int_{y_1} \dots \int_{y_n} \left(\int_{\theta} l\,(\hat{\Theta},\theta)\, h_{\Theta|Y}(\theta|y)\, d\theta \right) \times g_Y(y)\, \mathrm{d}y_1 \dots \mathrm{d}y_n. \quad (A.9)$$

Now, the problem of minimizing $E\,[l(\hat{\Theta},\theta)]$ when $Y = y = (y_1, \dots, y_n)$ is equivalent to minimizing the following quantity:

$$K(\hat{\Theta}, y) := \int_{\theta} l(\hat{\Theta},\theta) h_{\Theta|Y}(\theta|y)\, \mathrm{d}\theta. \quad (A.10)$$

The function $K(\hat{\Theta}, y)$ is sometimes called the a posteriori *risk* for estimating Θ.

Let X be a $m \times 1$ random vector of parameters to be estimated. It is assumed that some a priori information on X be available, in the form of its mean and covariance matrix:

$$\mu_X := \mathbf{E}[X]. \quad (A.11)$$

$$\mathbf{V}_{XX} := \mathbf{E}[(X - \mu_X)\,(X - \mu_X)^{\mathrm{T}}]. \quad (A.12)$$

This information on X must be updated by means of some observations on an $n \times 1$ random vector Y, which is linearly related to X as follows:

$$Y = \mathbf{H}X + U, \quad (A.13)$$

where:

- $\mathbf{H}$ is an $n \times m$ known mapping matrix of rank $m \leqslant n$, whose components are h_{ki}.
- U is a 1×1 random vector, called noise or error, due to imperfection of the observations such that:

$$\mathbf{E}[U] = 0, \quad (A.14a)$$

$$\mathbf{E}[UU^{\mathrm{T}}] = \mathbf{V}, \quad (A.14b)$$

$$\mathbf{E}[UX^{\mathrm{T}}] = \mathbf{0}. \quad (A.14c)$$

Let us consider the class of linear estimators defined by the formula:

$$\hat{X} = \mathbf{a} + \mathbf{A}\,Y, \quad (A.15)$$

where $\mathbf{a}$ is a vector of real numbers, and $\mathbf{A}$ is a real matrix, selected so that:

$$\mathbf{E}[\hat{X} - X] = 0 \quad (A.16a)$$

and

$$\mathbf{Q} = \mathbf{E}[(\hat{X} - X)\,(\hat{X} - X)^{\mathrm{T}}] \quad (A.16b)$$

is minimized.

Condition (A.16a) requires that the estimator is unbiased (see Definition 5). The minimization of $\mathbf{Q}$ in Eq. (A.16b) corresponds to the minimization of the matrix-valued loss function:

$$\mathbf{L}(\hat{X}, X) = \mathbf{E}[(\hat{X} - X)\,(\hat{X} - X)^{\mathrm{T}}] \quad (A.17)$$

according to Definitions 6 and 7, where minimization is in the sense specified by Dwyer and Macphail [34].

Gauss–Markov Theorem . *Let* $\mathbf{a} + \mathbf{A}Y$ *be an estimator of* X *in the linear model (A.13). Then the optimum values of* $\mathbf{a}$ *and* $\mathbf{A}$ *for which* $\mathbf{Q}$ *in Eq. (A.16b) is minimum are:*

$$\mathbf{a} = \mu_X - \mathbf{A}^*\mathbf{H}\mu_X. \quad (A.18)$$

$$\mathbf{A}^* = \mathbf{V}_{XX}\mathbf{H}^{\mathrm{T}}(\mathbf{H}\mathbf{V}_{XX}\mathbf{H}^{\mathrm{T}} + \mathbf{V})^{-1}. \quad (A.19)$$

The covariance matrix of the estimator is:

$$\mathbf{V}_{\hat{X}} = \mathbf{A}^*\mathbf{H}\mathbf{V}_{XX}. \quad (A.20)$$

Upon substitution of Eq. (A.19) into Eq. (A.18), the estimator may be written as:

$$\hat{X} = \mu_X + \mathbf{A}^*(Y - \mathbf{H}\mu_X). \quad (A.21)$$

References

[1] Brady BHG, Brown ET. Rock mechanics for underground mining, 2nd ed. London: Chapman & Hall, 1993.

[2] Amadei B, Stephanson O. Rock stress and its measurement. London: Chapman & Hall, 1997.

[3] Barla G, Gioda G. Un esempio di interpretazione delle misure di convergenza in galleria. In: Proc. XV Convegno Nazionale di Geotecnica. Spoleto, Italy, May 4–6, 1983. p. 281–86.

[4] Purrer W. Geotechnical based procedures in tunneling. Felsbau 1997;15(3):222–4.

[5] Gelman A, Carlin JB, Stern HS, Rubin DB. Bayesian data analysis. London: Chapman & Hall, 1995.

[6] Einstein HH, Baecher GB. Probabilistic and statistical methods in engineering geology: Specific Methods and Examples. Part 1: exploration. Rock Mech Rock Eng 1983;16:39–72.

[7] Cornet FH. Stresses in rock, rock masses. In: Hudson JA, editor. Comprehensive Rock Engineering, Oxford: Pergamon Press, 1993;3:297–327.

[8] Cornet FH. The HTPF, The integrated stress determination methods. In: Hudson JA, editor. Comprehensive Rock Engineering, Oxford: Pergamon Press, 1993;3: 413–32.

[9] Tarantola A, Valette B. Generalized non-linear inverse problem solved using the least squares criterion. Rev Geophys Space Phys 1982;20:219–32.

[10] Wiles TD, Kaiser PK. In situ stress determination using the under-excavation technique-I. Theory. Int J Rock Mech Min Sci Geomech Abstr 1994;31(5):439–46.

[11] Wiles TD, Kaiser PK. In situ stress determination using the under-excavation technique-II. Applications. Int J Rock Mech Min Sci Geomech Abstr 1994;31(5):447–56.

[12] Menke W. Geophysical data analysis: discrete inverse theory. San Diego: Academic Press, 1989.

[13] Gioda G, Maier G. Direct search solution of an inverse problem in elastoplasticity: identification of cohesion, friction angle and in situ stress by pressure tunnel tests. Int J Num Methods Eng 1980;15:1823–48.

[14] Sakurai S. Lessons learned from field measurements in tunnelling. Tunnelling Underground Space Technol 1997;12(4):453–60.

[15] Cividini A, Maier G, Nappi A. Parameter estimation of a static geotechnical model using a Bayes' approach. Int J Rock Mech Min Sci Geomech Abstr 1983;20(5):215–26.

[16] Towse DF, Heuze FE. Estimating in situ stresses and rock mass properties from geological and geophysical data: applications in the hydraulic fracturing of tight gas reservoirs. Lawrence Livermore National Laboratories, UCRL-53443, University of California, Livermore, CA, 1983.

[17] Telford WM, Geldart LP, Sheriff RE. Applied geophysics, 2nd ed. Cambridge: Cambridge University Press, 1990.
[18] Tarantola A. Inverse problem theory: methods for data fitting and model parameter estimation. New York: Elsevier, 1987.
[19] Mase GE. Continuum mechanics. New York: McGraw-Hill, 1970.
[20] Jaynes ET. Information theory, statistical mechanics. Phys Rev 1957;106/108:620–630; 171–190. Reprinted In: Rosenkranz RD editor. Papers on probability, statistics and statistical physics. Dordrecht: Reidel, 1983.
[21] Jaynes ET. Prior probabilities. IEEE Trans Syst Sci Cybernet 1968;SSC-4:227–241. Reprinted In: Rosenkranz RD, editor. Papers on probability, statistics and statistical physics. Dordrecht: Reidel, 1983.
[22] Jaynes ET. Papers on probability, statistics and statistical physics. In: Rosenkranz RD, editor. Dordrecht: Reidel, 1983.
[23] G + D Computing, Strand7 User's Manual. G + D Computing Pty Ltd., Sydney, 1999. www. strand.aust.com/strand7.
[24] Tonon F. Three-dimensional Modeling of Underground Excavations and Estimation of Boundary Conditions in Rock with Fabric. Ph.D. dissertation, University of Colorado at Boulder, 2000.
[25] Tonon F, Amadei B, Frangopol DM. Estimation of rock mass boundary conditions using a Bayesian approach—Application to the URL, Canada. In: Yufin SA, editor. Proceedings of the Third International Conference Advances of Computer Methods in Geotechnical and Geoenvironmental Engineering, The Netherlands: Balkema, Rotterdam, 2000. p. 67–72.
[26] Tonon, F, Amadei, B, Frangopol, DM, Estimation of boundary conditions in tunneling using a Bayesian approach. In: Kareem A, Haldar A, editors. Proceedings of the Eighth ASCE Joint Specialty Conference on Probabilistic Mechanics and Structural Reliability, 2000. ASCE, Reston, VA, Paper 253.
[27] Collins JD, Hart GC, Hasselmann TK, Kennedy B. Statistical identification of structures. AIAA J 1974;12:185–90.
[28] Beliveau JG. Identification of viscous damping in structures from modal information. J Appl Mech 1976;18:335–9.
[29] Isenberg J, Collins JD, Kavarna J. Statistical estimations of geotechnical material model parameters from in situ test data. In: Ang AH-S, Shinozuka M, editors. Proceedings ASCE Special Conference On Probabilistic Mechanics and Structural Reliability. New York: ASCE, 1979. p. 348–52.
[30] Hart GC, Torkamani MAM. Structural system identification. In Stochastic Problem in Mechanics, University of Waterloo, 1977.
[31] Tonon F, Amadei B, Pan E. Bayesian estimation of boundary conditions with applications to deep tunneling. Geotech Geol Eng 2001;19:43–67.
[32] Ang AH-S, Tang WH. Probability concepts in engineering planning and design, vol. 1. New York: John Wiley & Sons, 1975.
[33] Lewis TO, Odell PL. Estimation of linear models. Englewood Cliffs, NJ: Prentice-Hall, 1971.
[34] Dwyer PS, Macphail M. Symbolic matrix derivatives. Ann Math Statist 1948;XIX:517–34.
[35] Herget G. Rock stresses and rock stress monitoring in Canada. In: Hudson JA, editor. Comprehensive Rock Engineering, vol. 3. Oxford: Pergamon Press, 1993. p. 473–96.
[36] Martino JB, Thompson PM, Chandler NA, Read RS. The in situ Stress Program at AECL's Underground Research Laboratory—15 Years of Research (1982–1997). Report no. 06819-REP-01200-0053 R00. Atomic Energy of Canada Ltd., Whitshell laboratories, Canada, 1997.
[37] Brown A, Soonawala NM, Everitt RA, Kamineni DC. Geology and geophysics of the Underground Research Laboratory Site, Lac du Bonnet Batholith, Manitoba. Can J Earth Sci 1989; 26:404–25.
[38] Everitt RA, Brown A, Davison C, Gascoyne M, Martin CD. Geological and hydrogeological setting of the Underground Research Laboratory. In: Sinha RS, editor. Proceedings of the International Symposium Unique Underground Structures, vol. 2. Denver, CO: CSM Press, Denver, 1990. p. DO. 64: 1–64:23.
[39] Stone D, Kamineni DC. Structural analysis of the thrust fault at a depth of 271 to 275 m in the Underground Research Laboratory shaft. Atomic Energy Canada Limited Technical Record, TR-461*, 1988.
[40] Davison CC. Hydrogeological characterization at the site of Canada's Underground Research Laboratory. Proceedings of the IAH International Symposium on Groundwater Resource Utilization and Contaminant Hydrogeology, Montreal, Canada, 1984. p. 310–35.
[41] Jackson R, Lau JSO, Annor A. Mechanical, thermo-mechanical and joint properties of rock samples from the site of AECL's Underground Research Laboratory, Lac du Bonnet, Manitoba. Proceedings of the 42nd Canadian Geotechnical Conference, Materials from Theory to Practice, Winnipeg, Canada, 1989. p. 41–49.
[42] Chernis PJ. Comparison of the pore-microstructure of shallow, deep samples of the Lac du Bonnet granite. Atomic Energy of Canada Limited Technical Record TR-223*, 1984.
[43] Katsube TJ, Hume JP. Geotechnical studies at Whiteshell Research Area (RA-3). Canada Centre for Mineral and Energy Technology Mining Research Laboratories Divisional Report, Report No. MRL 87–52, 1987.
[44] Martin CD, Simmons GR. The atomic energy of Canada limited underground research laboratory: an overview of geomechanics characterization. In: Hudson JA, editor. Comprehensive Rock Engineering, vol. 5. Oxford: Pergamon Press, 1993. p. 915–50.
[45] Mammino A, Tonon F. Opere Strutturali per l'Ingegneria Territoriale, vol. 1. Tome 2. Alinea Editrice, Firenze, Italy, 1997.
[46] Barton NR, Bandis SC. Effects of block size on the shear behavior of jointed rock. In: Goodman RE, Heuze FE, editor. Proceedings of the 23rd US Symposium on Rock Mechanics, Berkeley, CA, 1983. Am Soc Min Eng, New York. p. 739–60.
[47] Hoek E, Brown ET. Underground excavations in rock. London: Institution of Mining and Metallurgy, 1980.
[48] Hart RD. An introduction to distinct element modeling for rock engineering. In: Comprehensive Rock Engineering, vol. 2. Oxford: Pergamon Press, 1993. p. 245–61.
[49] Kulhawy FH. Stress deformation properties of rock and rock discontinuities. Eng Geol 1975;9:327–50.
[50] Rosso RS. A comparison of joint stiffness measurements in direct shear, triaxial compression, and in situ. Int J Rock Mech Min Sci Geomech Abstr 1976;13:167–72.
[51] Bandis SC, Lumdsen AC, Barton NR. Fundamentals of rock joint deformation. Int J Rock Mech Min Sci Geomech Abstr 1983;20(6):249–68.
[52] Hoek E, Brown ET. Practical estimates of rock mass strength. Int J Rock Mech Min Sci 1997;34(8):1165–86.
[53] Barden L. Stresses and displacements in a cross-anisotropic soil. Géotechnique 1963;13:198–210.
[54] Martin CD,, Chandler NA. Stress heterogeneity and geological structures. Int J Rock Mech Min Sci Geomech Abstr 1993;30(7):993–9.
[55] Herget G. Arjang B. Update on ground stresses in the Canadian Shield. In: Herget G, editor. Proceedings of the Stresses in Underground Structures. Ontario, Ottawa (Canada): Energy, Mines and Resources, 1990. p. 33–47.
[56] Martin CD, Christiansson R. Overcoring in highly stressed granite-the influence of microcracking. Int J Rock Mech Min Sci Geomech Abstr 1991;28(1):53–70.

[57] Haimson B, Lee M, Chandler N, Martin D. Estimating the state of stress from subhorizonal hydraulic fractures at the underground research laboratory, Manitoba. Int J Rock Mech Sci Geomech Abstr 1993;30(7):959–64.
[58] Corthésy R, Gill DE, Leite MH, Thompson PM. Stress measurements in high-stress zones using the modified doorstopper technique. Can Geotech J 1993;30:991–1002.
[59] Martino JB. Distometer convergence readings in the shaft extension of Atomic Energy of Canada Limited's Underground Research Laboratory. Atomic Energy Canada Limited Technical Record, TR-482*, 1989.
[60] Kaiser PK. Wiles TD. Zou D. Two- and three-dimensional stress back-analysis. Report to Atomic Energy of Canada Limited under contract WS-29J-54460, Laurentian University, 1991.
[61] Wiles TD, Kaiser PK. Under-excavation method incremental analysis of 420 Level vent raise and Room 209 data. Contractor's report to Atomic Energy of Canada Limited, Laurentian University, Canada, 1992.
[62] Read RS, Martin CD. Technical Summary of AECL's Mine-by Experiment Phase 1: Excavation Response. Whiteshell Laboratory, Pinawa, Manitoba R0E 1L0, Canada, 1996.
[63] Talebi S, Young RP. Microseismic monitoring in highly stressed granite: relation between shaft-wall cracking and the in situ stress. Int J Rock Mech Min Sci Geomech Abstr 1992; 29(1):25–34.
[64] Curran JH, Corkum BT. Phase2. 2D finite element program for calculating stresses and estimating support around underground excavations. Reference Manual and Tutorial Manual. Rockscience, Toronto, Canada, 1998.
[65] Angelier J. From orientation to magnitudes in paleostress determinations using fault slip data. J Struct Geol 1989;11(1/2): 37–50.
[66] Angelier J, Tarantola A, Valette B, Manoussis S. Inversion of field data in fault tectonics to obtain the regional stress—I Single phase fault populations: a new method of computing the stress tensor. Geophys J R Astr Soc 1982;69:607–21.
[67] Chandler NA. Personal communication. 1999.
[68] Golden Software, Surfer User's Manual. Golden Software, Golden, CO, 1997.
[69] Cornet FH. Stresses in rock and rock masses. In: Hudson JA, editor. Comprehensive Rock Engineering, Oxford: Pergamon Press, vol. 3, 1993. p. 297–327.